

Recent advances in heteroatom substitution $\text{Sr}_2\text{Fe}_{1.5}\text{Mo}_{0.5}\text{O}_{6-\delta}$ oxide as a more promising electrode material for symmetrical solid-state electrochemical devices: A review

Received: 02 July 2022
Accepted: 25 September 2022

Natalia Porotnikova ^{a*}, Denis Osinkin ^{bc}

DOI: [10.15826/elmattech.2022.1.003](https://doi.org/10.15826/elmattech.2022.1.003)

In recent years, the interest in solid state electrochemical devices has significantly increased due to the various cases of their use in the energy field. The first case is the solid oxide fuel cells with both oxygen-ion and proton-conducting membranes. The second case is the electrolysis cells for hydrogen production. As a rule, in both cases, electrochemical cells consist of an ion-conducting membrane and two different electrodes. The present review is focused on structural, physicochemical, and electrochemical properties of a complex oxide based on strontium ferrite with partial replacement of iron by molybdenum. This complex oxide has a number of unique characteristics: in particular, it is able to function effectively as an electrode in oxidizing and strongly reducing atmospheres, which makes it a promising material for electrochemical devices based on solid electrolytes with symmetrical electrodes. Doping with elements in A-, B- and O-sublattices and surface modification increases electro-catalytic activity of $\text{Sr}_2\text{Fe}_{1.5}\text{Mo}_{0.5}\text{O}_{6-\delta}$ porous oxide material, which increases competitiveness of the electrode material for application in solid oxide electrochemical devices. Mechanisms for improving electro-catalytic activity are outlined stepwise by doping of different sublattices of double perovskite, by level of doping, and by different types of dopants. In conclusion, the data on material conductivity, power densities of both symmetric and fuel cells are systematized, and the remaining problems and prospects for future developments and upgrades of $\text{Sr}_2\text{Fe}_{1.5}\text{Mo}_{0.5}\text{O}_{6-\delta}$ oxide electrode material are described.

keywords: $\text{Sr}_2\text{Fe}_{1.5}\text{Mo}_{0.5}\text{O}_{6-\delta}$, IT-SOFCs, anode materials, cation doping, conductivity, anion doping, polarization resistance, symmetrical electrode

© 2022, the Authors. This article is published in open access under the terms and conditions of the Creative Commons Attribution (CC BY) license <http://creativecommons.org/licenses/by/4.0/>.

1. Introduction

Methods of production, storage, transportation, and use of hydrogen are among the main directions of science and technology development [1–3]. A good trend in this area is the development of solid oxide fuel cells

(SOFCs) and power generation system based on them. SOFCs are direct converters of fuel chemical energy into electricity and have a series of undeniable advantages over traditional methods of generating electricity [4]. Classical SOFC is an ion-conducting membrane (solid zirconium oxide electrolyte) and two electrodes separated by this membrane, cathode is an oxygen electrode and anode is a fuel electrode. Traditionally, solid oxide fuel cell electrodes are cathode, which consists of oxides with mixed oxygen-electron conductivity [5–8]; and anode, which is a composite material based on nickel and ceramics (Ni cermets) [9–11]. Such fuel cells have proven to perform well with hydrogen as a fuel in the temperature range of 800–900°C. However, lower

- a: Laboratory of Cross-Cutting Technologies in Distributed Power Generation, Institute of High-Temperature Electrochemistry, Yekaterinburg 620066, Russia
- b: Laboratory of Solid State Oxide Fuel Cells, Institute of High-Temperature Electrochemistry, Yekaterinburg 620066, Russia
- c: Department of Environmental Economics, Graduate School of Economics and Management, Ural Federal University, Yekaterinburg 620002, Russia

* Corresponding author: porotnikova@ihte.uran.ru

operating temperatures and/or the use of gaseous hydrocarbons (methane, propane, etc.) and natural or synthesis gas in such SOFCs is difficult because of the increase in the ohmic resistance of the zirconium electrolyte and the formation of carbon on the nickel-containing anode [12–14]. Another disadvantage of nickel-containing anodes is their rapid degradation in atmospheres with high water content [15, 16]. A new direction in the field of SOFC development is the research of electrochemical cells with identical, i.e., symmetrical electrodes [17–19]. Any complex oxides with high stability in a hydrogen atmosphere, such as manganites, chromites, and titanates of alkali earth metals and lanthanides, can theoretically be used as symmetric electrodes [20, 21]. However, these systems do not have the necessary properties for their practical application in the symmetrical SOFCs.

Of particular note is strontium ferrite, which, due to its electronic structure, is highly stable in reducing gas environments, even at high temperatures [22–25]. In addition, strontium ferrite has a thermal expansion comparable to traditional electrolyte materials [22]. A few years ago, papers were published on the use of doped strontium ferrite as electrodes for symmetric SOFCs. For example, the partial replacement of iron ions by molybdenum ions allows the electrical properties to be significantly increased due to the formation of the redox couple $\text{Fe}^{2+} + \text{Mo}^{6+} \rightarrow \text{Fe}^{3+} + \text{Mo}^{5+}$ and the formation of oxygen vacancies in the crystal lattice. Substitution of 25% of iron ions with molybdenum leads to the formation of oxide $\text{Sr}_2\text{Fe}_{1.5}\text{Mo}_{0.5}\text{O}_{6-\delta}$ (SFM). SFM is single-phase after synthesis in air and has a sufficient level of conductivity and electrochemical activity. It is chemically stable when in contact with the highly conductive lanthanum gallate-based electrolyte and can be considered as the main candidate for electrodes of symmetric electrochemical cells.

2. Properties and modification of the oxide

2.1. Structure and aspects of synthesis

The structure of strontium ferrite-molybdate can be considered as FeO_6 and MoO_6 octahedra alternating along the three directions of the crystal, with strontium cations occupying the space between the octahedra. Depending on the ordering of iron, molybdenum atoms, occupied and vacant oxygen atoms, the oxide has either a cubic $Pm\text{-}3m$ or tetragonal A/mmm crystal structure [26, 27], Figure 1.

The Goldschmidt tolerance factor can be useful for determining the stability of the perovskite phase for a certain array of anions and cations [28]. Cations A are

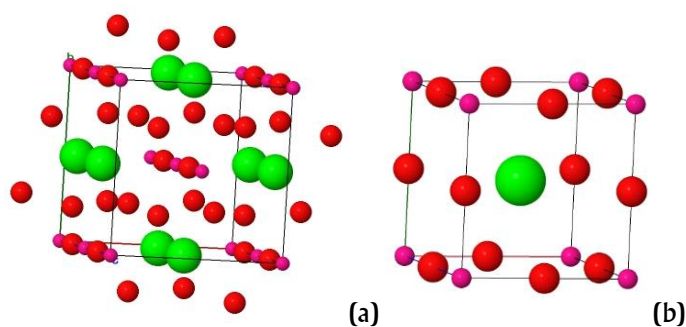


Figure 1 Schematic structure of $\text{Sr}_2\text{Fe}_{1.5}\text{Mo}_{0.5}\text{O}_{6-\delta}$ presented in space group A/mcm #140 (a) and $Pm\text{-}3m$ #221 (b), where Sr (green), Fe/Mo (red), O (magenta) [27] Copyright ©, Springer Materials.

coordinated with XII oxygen ions, and cations B and B' are coordinated with VI oxygen ions in the perovskite structure. The oxygen anions are coordinated by II cations of site B and IV cations of site A. For perovskites ABO_3 , the equation is as follows:

$$t = \frac{R_A + R_O}{\sqrt{2}(R_B + R_O)} \quad (1)$$

where R_A , R_B , R_O are ionic radii for ions in A, B, O sites. The tolerance factor for hexagonal or tetragonal structures has the value $t > 1$, for cubic structure the value is 0.9–1, for orthorhombic or rhombohedral structures – 0.71–0.9. When the B-cation is doped with another cation, the radii are substituted depending on the concentration of the ion in the structure.

The tolerance factor can be used to estimate the stability of the perovskite phase during doping in both cation and anion sublattices. Often the structure can differ with the same group of ions, which may be due to the non-stoichiometric nature of the compound. This can be observed for $\text{Sr}_2\text{Fe}_{1.5}\text{Mo}_{0.5}\text{O}_{6-\delta}$, where the oxygen content in the structure can vary from 5.50 to 6.0 depending on the sintering conditions [27].

The ordering and occupancy of the B-sublattice in $\text{A}_2\text{BB}'\text{O}_6$ is controlled by the synthesis technique, and the occupancy has a significant influence on the material properties. The earliest studies of double perovskites date from the 1960s. Longo J. and Ward R. [29] showed that complex oxides can be obtained by solid-phase synthesis, where A = Ba, Sr, Ca, B = Fe, B' = Re. Grinded mixtures of simple oxide reagents were heat-treated in evacuated quartz capsules at 900–1000°C for 24 h. Compounds with barium and strontium were described by the tetragonal structure with cell parameters $a = 5.70 \text{ \AA}$, $c = 8.05 \text{ \AA}$ for $\text{Ba}_2\text{FeReO}_{6-\delta}$ and $a = 5.57 \text{ \AA}$, $c = 7.89 \text{ \AA}$ for $\text{Sr}_2\text{FeReO}_{6-\delta}$. The calcium compound $\text{Ca}_2\text{FeReO}_6$ was

described by the orthorhombic structure with cell parameters $a = 5.41 \text{ \AA}$, $b = 5.53 \text{ \AA}$, $c = 7.69 \text{ \AA}$.

Later, Galasso F.S. et al. [30] were first to describe the structure of A_2FeMoO_{6-6} type compounds, in which oxygen and large metal cations were tightly packed in the direction (III) with iron and molybdenum ions alternating in octahedral coordination between the oxygen layers, so that Fe-O-Mo bonds were at 180° and represented half an edge of the unit cell. Solid solutions of the ordered perovskite phases Ba_2FeMoO_{6-6} and Sr_2FeMoO_{6-6} were prepared by high-temperature annealing (1035°C) of the milled mixture in appropriate amounts of SrO, BaO, CaO, Fe_2O_3 , Mo and MoO_3 reagents. The authors claimed that the compositions were not single-phase at heat treatment in air. All compounds contained additional phases of $SrMoO_4$ and $BaMoO_4$. Ba_2FeMoO_{6-6} oxide had the cubic cell with a unit cell size $a = 8.0665 \text{ \AA}$. The authors recorded deviations from the 180° bond angle resulting in a distortion of the cubic lattice; the crystal structure of Sr_2FeMoO_{6-6} was described as a tetragonal unit cell. Nakagawa T. [31] confirmed that it was not possible to obtain single-phase material at ambient air, only in full vacuum silica capsules at temperature above 1100°C . Another method of producing oxides is sintering in a reducing atmosphere of 5% $H_2/95\%Ar$ (N_2) [32–35]. The very easy formation of $SrMoO_4$ during processing should also be a key difficulty in the complete synthesis of this phase. In a humid atmosphere, the double oxide decomposes predominantly to form simple oxide FeO and hydroxide $Sr(OH)_2$ and $SrMoO_4$ [33]. Using a non-classical solid-phase method, such as spark plasma sintering [36], microwave sintering [37], pulsed laser deposition [38], sol-gel method [39–42], and Pechini [43] methods, makes it possible to achieve single-phase at reduced temperatures in vacuum or a humid atmosphere. Consequently, Sr_2FeMoO_{6-6} in air is thermodynamically unstable due to insufficient Mo and Fe solubility in $SrFeO_{3-6}$ and $SrMoO_4$, respectively.

One of the most promising directions in the study of compounds with double perovskites Sr_2FeMoO_{6-6} is the reduction of molybdenum in the B-sublattice, which makes such compositions more thermodynamically stable. A homogeneous solid solution of $Sr_2Fe_{2-y}Mo_yO_{6-6}$ is formed at 1200°C in air with the addition of molybdenum to $y = 0.6$ in the double perovskite structure [33, 44]. The $SrMoO_4$ and $SrFeO_{3-6}$ phases are formed at high molybdenum concentrations, which are formed at an excess of $y > 0.6$. The composition with $y = 0.5$ is the most popular because of its ability to be

synthesized in air, its stability and good conductivity characteristics.

Mostly $Sr_2Fe_{1.5}Mo_{0.5}O_{6-6}$ phase was synthesized by solid-phase method by mixing initial oxides and/or carbonates [27, 45–48], or by sol-gel synthesis where nitrate salts and complexes were used as initial reagents followed by dissolution in deionized water with addition of glycine and citric acid [45, 49–54]. The $Sr_2Fe_{1.5}Mo_{0.5}O_{6-6}$ oxide has a primitive cubic $Pm\bar{3}m$ structure [20, 38, 49, 55, 56] after sintering in air, cubic face-centered $Fm\bar{3}m$ structure [45, 52, 57–59] also after sintering in air, and tetragonal A/mcm or A/m structure [27, 47, 50] after treatment in hydrogen. The unit cell parameters, synthesis methods and conditions are given in Table 1. The gas environment during annealing significantly affects the occupancy of the oxygen sublattice, resulting in structural distortions and changes in the crystal lattice.

The introduction of aliovalent ions into the A- and/or B-sublattices also leads to changes in the crystal structure [52, 60–62]. The increase of Ba content in $Sr_{2-x}Ba_xFe_{1.5}Mo_{0.5}O_{6-6}$ leads to lattice expansion due to the larger ion radius of Ba^{2+} (1.61 \AA) compared to Sr^{2+} (1.44 \AA). The stability of the perovskite crystal structure gradually worsens according to the calculations of the tolerance factor; the single-phase oxide is retained up to $x = 0.8$, phase separation occurs above this value, with the formation of $BaMoO_4$, Fe, SrO and BaO [52, 60]. The reduction of Fe oxidation degree at partial heterovalent substitution of Sr^{2+} by La^{3+} and Fe^{3+} by Co^{2+} in $Sr_{2-x}La_xFe_{1-y}Co_yMo_{0.5}O_{6-6}$ leads to the increase of perovskite phase stability in H_2 at 1100°C ; phase stability is kept at $x = 0.4$, $y = 0.5$ [62].

Substitution of A- or B-sublattice ions with other types of cations is a common practice to optimize the performance of perovskite oxide systems. To increase the electrocatalytic activity, it is necessary to stabilize the structure of strontium ferrite-molybdates and improve the durability of the material in redox environments. Several studies have been carried out by doping the strontium A-sublattice with cations of alkali element (K), alkaline-earth elements (Ca, Ba), and rare-earth elements (La, Sm), or by forming a deficient in the A-sublattice. For the same purpose the modification of the B-sublattice with transition metals (Co, Cu, Ni, Nb, Mn, Ti, Sc, Ga, Zr, Bi, Al, Mg, Sb), noble metal (Ru), or O-sublattice anion doping (N, Cl, F) leads to a change in crystallinity and in electrochemical properties of the materials. The effects of $Sr_2Fe_{1.5}Mo_{0.5}O_{6-6}$ doping will be described in more detail in the following chapters.

2.2. Complex oxide Sr₂Fe_{1.5}Mo_{0.5}O_{6-δ}

Sr₂Fe_{1.5}Mo_{0.5}O_{6-δ} oxide demonstrates high electronic conductivity under reducing conditions due to the degeneration and hybridization of coexisting states Fe³⁺/Mo⁵⁺ ↔ Fe²⁺/Mo⁶⁺. Although the total concentration of Fe and Mo atoms is well controlled, it is much more difficult to control the distribution of Fe and Mo atoms in the two alternating lattices during synthesis [63]. In fact, all samples contain a certain amount of vacancy defects, where some Fe atoms exchange positions with Mo atoms. Usually, these defects are randomly distributed, and their number characterizes the degree of Fe/Mo ordering in the sample, which can be determined by X-ray diffraction [64]. The use of functional density

theory demonstrates that a higher concentration of oxygen vacancies is expected in Sr₂FeMoO_{6-δ} at the Fe/Mo > 1 ratio, the presence of vacancies should accelerate the diffusion of oxide ions and can also improve the electronic conductivity based on electron delocalization during vacancy formation [65]. Vacancies along Fe–O–Fe are preferred with respect to those along Mo–O–Fe or Mo–O–Mo due to weaker Fe–O bonds and preferential delocalization of the extra charge left after vacancy formation (due to the driving force to retain a half-filled Fe d-shell), which also acts to preserve high electronic conductivity in Sr₂Fe_{1.5}Mo_{0.5}O_{6-δ} [66]. Density functional theory (DFT)-based first-principles calculations show that hydrogen molecule exhibits weak physical adsorption behavior,

Table 1 – Synthesis conditions, type, and lattice parameters of A, B-doped Sr₂Fe_{1.5}Mo_{0.5}O_{6-δ}.

Oxide	Method of synthesis	Conditions of synthesis	Unit cell parameters	Space group, structure	Ref.
Sr ₂ Fe _{1.5} Mo _{0.5} O _{6-δ}	solid state reaction	1200°C, 12h in air	<i>a</i> = 5.5548(2) Å, <i>c</i> = 7.8783(5) Å	<i>A</i> / <i>mcm</i> , tetragonal	27
Sr ₂ Fe _{1.5} Mo _{0.5} O _{6-δ}	solid state reaction	1200°C, 12h in air, 850°C, 4% H ₂ /He	<i>a</i> = 3.9794(1) Å	<i>Pm</i> -3 <i>m</i> , cubic	27
Sr ₂ Fe _{1.5} Mo _{0.5} O _{6-δ}	solid state reaction	1200°C, 12h in air	<i>a</i> = 7.8717(1) Å	<i>Fm</i> -3 <i>m</i> , Cubic	45
Sr ₂ Fe _{1.6} Mo _{0.4} O _{6-δ}	solid state reaction	1200°C, 12h in air	<i>a</i> = 3.905(1) Å	<i>Pm</i> -3 <i>m</i> , cubic	46
Sr ₂ Fe _{1.5} Mo _{0.5} O _{6-δ}	microwave-combustion method	1200°C, 12h in air	<i>a</i> = 3.92874(6) Å	<i>Pm</i> -3 <i>m</i> , cubic	49
Sr ₂ Fe _{1.5} Mo _{0.5} O _{6-δ}	sol-gel method	1250°C, 12h in air	<i>a</i> = 5.54301(15) Å, <i>c</i> = 7.8471(4) Å	<i>A</i> / <i>mcm</i> , tetragonal	50
Sr ₂ Fe _{1.5} Mo _{0.5} O _{6-δ}	citrate method	1100°C, 5h in air	<i>a</i> = 3.92719 Å	<i>Pm</i> -3 <i>m</i> , Cubic	51
Sr ₂ Fe _{1.5} Mo _{0.5} O _{6-δ}	solution combustion method	1200°C, 6h in air	<i>a</i> = 7.8664 Å	<i>Fm</i> -3 <i>m</i> , Cubic	52
Sr _{2-x} Ba _x Fe _{1.5} Mo _{0.5} O _{6-δ} (<i>x</i> = 0.3–0.9)	solution combustion method	1200°C, 6h in air	<i>a</i> = 7.8664 Å content BaO	<i>Fm</i> -3 <i>m</i> , Cubic	52
Sr _{2-x} Ba _x Fe _{1.5} Mo _{0.5} O _{6-δ} (<i>x</i> = 0–0.8)	citrate combustion method	1100°C, 5h in air, 800°C, 2h in H ₂	<i>a</i> = 7.8664– 7.9309 Å	<i>Fm</i> -3 <i>m</i> , Cubic	60
Sr ₂ Fe _{0.75} Ti _{0.25} MoO _{6-δ}	solid state reaction	1350°C, in air	<i>a</i> = 5.3711 Å, <i>c</i> = 11.9823 Å	<i>A</i> / <i>m</i> , tetragonal	61
Sr ₂ FeCo _{0.5} Mo _{0.5} O _{6-δ}	sol-gel method	1100°C, 5h in air	<i>a</i> = 7.80824(8) Å	<i>Fm</i> -3 <i>m</i> , Cubic	62
Sr _{1.8} La _{0.2} FeCo _{0.5} Mo _{0.5} O _{6-δ}	sol-gel method	1100°C, 5h in air	<i>a</i> = 7.82224(9) Å	<i>Fm</i> -3 <i>m</i> , Cubic	62

while hydrogen atom strongly chemisorbed on SFM (001) surface [67, 68]. Hydrogen molecule preferably dissociates at surface (Fe)–Fe–(Fe) site with an activation barrier of 0.69 eV. Hydrogen oxidation on Sr₂Fe_{1.5}Mo_{0.5}O_{6-δ} (001) surface is favourable both in kinetics and thermodynamics, and the resulting desorption of H₂O molecules requires overcoming an energy barrier of 0.22–0.24 eV. Diffusion of oxygen atoms from volume to the surface prefers to follow the path from sub-surface (Fe)–O–(Fe) site to outer-surface (Fe)–Vo–(Mo) vacancy site, which requires crossing an energy barrier of 0.49 eV. The rate-limiting step of hydrogen conversion on the Sr₂Fe_{1.5}Mo_{0.5}O_{6-δ} surface is

determined to be hydrogen dissociation at temperature below 775°C and the hydrogen adsorption at temperature above 775°C. Stochastic surface models with different Fe/Mo ratios and oxygen vacancies in the gas surface layer are described to determine the active site and electro-oxidation mechanism for CO and a mixture of CO and H₂ [69]. The calculated current densities demonstrate that Sr₂Fe_{1.5}Mo_{0.5}O_{6-δ} anodes exhibit lower efficiency for CO compared to H₂ fuel, and the surface with a higher concentration of Mo in the upper layer exhibits higher activity for both fuels.

As described above, the iron-enriched system can be obtained in air at 1000°C in a cubic structure, with

$a = 7.8447(1) \text{ \AA}$, $V = 482.759(3) \text{ \AA}^3$, and space group $Fm\bar{3}m$ [70]. According to the results of photoelectron spectroscopy, the major oxidation states are of Sr^{2+} , Fe^{2+} , and Mo^{6+} . However, there should be an accompanying small portion of $\text{Fe}^{3+}/\text{Mo}^{5+}$ [70, 71]. Therefore, the calculated oxygen atoms in the $\text{Sr}_2\text{Fe}_{1.5}\text{Mo}_{0.5}\text{O}_{6-6}$ lattice should be between 5 and 5.75. Consequently, $\text{Sr}_2\text{Fe}_{1.5}\text{Mo}_{0.5}\text{O}_{6-6}$ is an oxygen deficient system with substantial oxygen vacancies. Model calculations of oxygen nonstoichiometry from temperature and oxygen pressure are shown in Figure 2(a), as well as a model of vacancy formation in the structure [72]. Three surface models with different Fe/Mo ratios in the outer layer, identified by *ab initio* thermodynamic analysis, are used to investigate the H_2 oxidation mechanism. A microkinetic analysis, which takes into account the influence of the anode bias potential, suggests that a higher Mo concentration in the surface increases the activity of the surface toward $\text{H}_2/\text{H}_2\text{O}$ oxidation [73,74] and has a high tolerance to sulfur poisoning [75, 76]. Figure 2(b) demonstrates the temperature dependence of conductivity of $\text{Sr}_2\text{Fe}_{1.5}\text{Mo}_{0.5}\text{O}_{6-6}$ in hydrogen and air [70]. At a maximum temperature of 780°C , the conductivity values are 550 S/cm in air and 310 S/cm in hydrogen, which are high values for a mixed conductor. The addition of CuO , NiO makes it possible to significantly increase the electrical conductivity of $\text{Sr}_2\text{Fe}_{1.5}\text{Mo}_{0.5}\text{O}_{6-6}$ -based anode materials in moist hydrogen by improving the grain boundary conductivity [77, 78]. The introduction of Fe_2O_3 slightly changes the overall conductivity of the material, but significantly affects the oxygen diffusion in the near-surface area by reducing the oxygen diffusion coefficient [79]. Electrical conductivity relaxation measurement demonstrates that the surface exchange coefficient of SFM is significantly improved by $\text{Ce}_{0.8}\text{Sm}_{0.2}\text{O}_{1.9}$ nanoparticles, from 10^{-5} to $10^{-3} \text{ cm}^2/\text{s}$ at 750°C [80].

$\text{Gd}_{0.2}\text{Ce}_{0.8}\text{O}_{1.9}$ nanoparticles were infiltrated onto the SFM surface to construct a composite GDC-SFM cathode and improve the CO_2RR performance in SOEC [81]. The current density over the GDC infiltrated SFM cathode with a GDC loading of 12.8 wt% reaches 0.446 A/cm^2 at 1.6 V and 800°C , which is much higher than that over the SFM cathode (0.283 A/cm^2). Temperature-programmed desorption of CO_2 measurements suggest that the infiltration of GDC nanoparticles significantly increases the density of surface-active sites and three phase boundaries, which are beneficial for CO_2 adsorption and subsequent conversion.

The performance of a $\text{La}_{0.9}\text{Sr}_{0.1}\text{Ga}_{0.8}\text{Mg}_{0.2}\text{O}_3$ electrolyte supported symmetrical fuel cell with the

configuration of SFM|LSGM|SFM was tested in wet H_2 (3 vol% H_2O) and CH_4 fuels [70]. The open circuit voltage (OCV) of the cell was 1.07 V at 900°C using wet H_2 , close to the value calculated from the Nernst equation. The OCV of the cell using wet (3 vol.% H_2O) CH_4 as fuel was 0.90 V at 900°C . The maximum power densities, Figure 2(c), at 900°C in wet H_2 and CH_4 are 835 and 230 mW/cm^2 , respectively. The kinetics of hydrogen oxidation on $\text{Sr}_2\text{Fe}_{1.5}\text{Mo}_{0.5}\text{O}_{6-6}$ electrode in contact with electrolyte $\text{La}_{0.85}\text{Sr}_{0.15}\text{Ga}_{0.85}\text{Mg}_{0.15}\text{O}_3$ was investigated in [82]. The hydrogen oxidation rate is determined by the low rate of oxygen heterogeneous exchange and slow dissociation of hydrogen on the $\text{Sr}_2\text{Fe}_{1.5}\text{Mo}_{0.5}\text{O}_{6-6}$ surface. At 800°C , the rates of these processes are comparable; with temperature decrease the rate of hydrogen oxidation is mainly limited by hydrogen dissociation. Decorating the $\text{Sr}_2\text{Fe}_{1.5}\text{Mo}_{0.5}\text{O}_{6-6}$ electrode with Ni-particles significantly increases the rate of hydrogen dissociation and increases the activity of the electrode more than two-fold.

There is an improving technique for fabricating a symmetrical cell, which increases power density and cell performance. The technique consists of fabricating a tri-layer porous/dense/porous LSGM structure with open pores, which are impregnated with a paste containing nanoscale particles [83–85]. The resulting symmetrical fuel cells produce maximum power densities of 703, 602, 521 and 401 mW/cm^2 at 800, 750, 700 and 650°C , respectively [84]. The subsequent impregnation of the electrodes with nanoscale Pr_6O_{11} catalyst allows for an increase in the electrochemical performance [86]. After the impregnation of electrodes Pr-SFM|GDC|YSZ|GDC|Pr-SFM in the symmetrical fuel cell, the polarization resistance is reduced by 47% to 0.10 S/cm^2 for the anode and by 80% to 0.021 S/cm^2 for the cathode; the maximum power density improves by 51% at 800°C . There is also a simple one-step co-sintering method for making symmetrical solid oxide fuel cells from $\text{Sm}_{0.2}\text{Ce}_{0.8}\text{O}_{1.9}$ electrolyte and $\text{Sr}_2\text{Fe}_{1.5}\text{Mo}_{0.5}\text{O}_{6-6}$ electrodes [87]. The single cell co-sintered at 1200°C possesses the highest peak power density of 216 mW/cm^2 at 700°C .

$\text{Sr}_2\text{Fe}_{1.5}\text{Mo}_{0.5}\text{O}_{6-6}$ (SFM) also has good reduction-oxidation (redox) stability [48, 49, 88–90]. Symmetrical electrolyzers with a cell configuration of 60wt%SFM–40wt% $\text{Sm}_{0.2}\text{Ce}_{0.8}\text{O}_{1.9}$ | $\text{La}_{0.8}\text{Sr}_{0.2}\text{Ga}_{0.8}\text{Mg}_{0.2}\text{O}_{3-6}$ are almost stable at a constant electrolysis current density of -0.060 A/cm^2 in 35h testing at 800°C , when the fuel electrode and oxygen electrode are exposed to 23% H_2O –77% N_2 and ambient air, respectively [88]. In [89] the electrochemical stability of $\text{Sr}_2\text{Fe}_{1.5}\text{Mo}_{0.5}\text{O}_{6-6}$

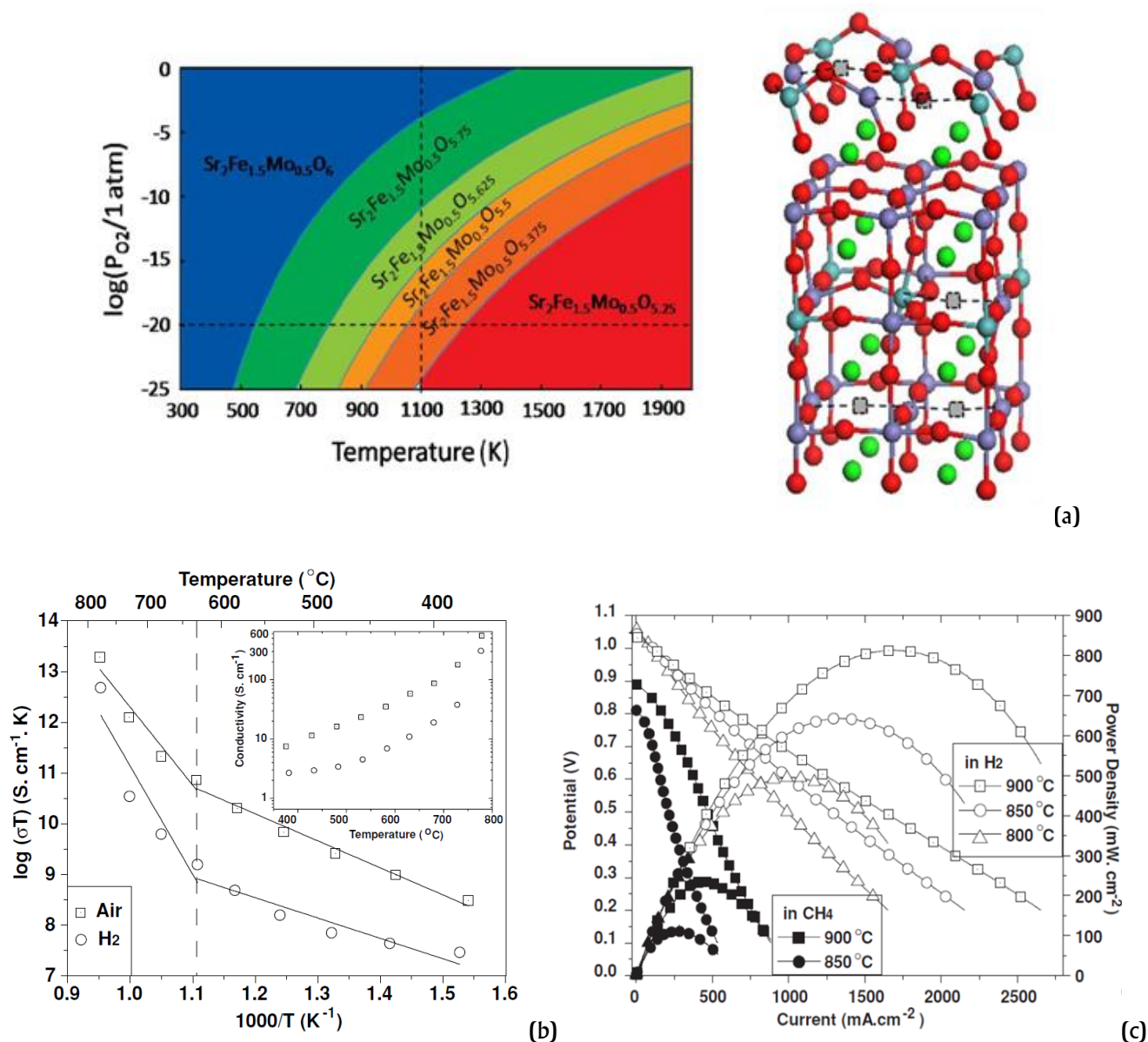


Figure 2 a) Theoretical non-stoichiometric phase diagram and presentation of oxygen vacancies in the structure of $\text{Sr}_2\text{Fe}_{1.5}\text{Mo}_{0.5}\text{O}_{6-\delta}$ [72]; b) Temperature dependencies of total conductivity of $\text{Sr}_2\text{Fe}_{1.5}\text{Mo}_{0.5}\text{O}_{6-\delta}$ in air and H_2 [70]; c) Performance of a symmetrical fuel cell SFM|LSGM|SFM with wet (3 vol. % H_2O) H_2 or CH_4 as fuel [70] Copyright © 2010 WILEY-VCH Verlag GmbH & Co. KGaA, Weinheim.

electrode was tested at 850 °C and 60 vol.% absolute humidity. A symmetrical cell with SFM| $\text{La}_{0.9}\text{Sr}_{0.1}\text{Ga}_{0.8}\text{Mg}_{0.2}\text{O}_3$ |SFM configuration was fabricated and operated at a constant cell voltage of 1.2 V. The cell current was recorded to evaluate the cell performance stability. After reaching the steady-state operation condition, no notable electrode passivation was observed during the subsequent 90 h electrolysis operations, indicating that SFM is relatively stable under high temperature and high humidity environment.

The regenerating characteristics of the SFM|LSGM|SFM symmetrical cell in $\text{H}_2/\text{H}_2+\text{H}_2\text{S}$, Figure 3(a), and H_2/CH_4 , Figure 3(b), have been evaluated using

cyclic tests [49]. After operation in H_2 with 100 ppm H_2S for 6 h at 800 °C, a reduction of 10% in performance was observed, indicating slight sulfur poisoning of the anode. After this regeneration treatment, the operability of the cell was almost completely restored. The process of sulfur poisoning and oxidative regeneration was repeated 5 times, and no obvious signs of permanent deactivation were observed. Prior to conducting the anode regenerative test in CH_4 , the fuel cell was operated using H_2 (with 3vol% H_2O) as the fuel for 15 h at 850 °C, and the stability of the cell performance was confirmed under these operating conditions. After operating the cell using H_2 as the fuel for 40 h, the anode regenerating

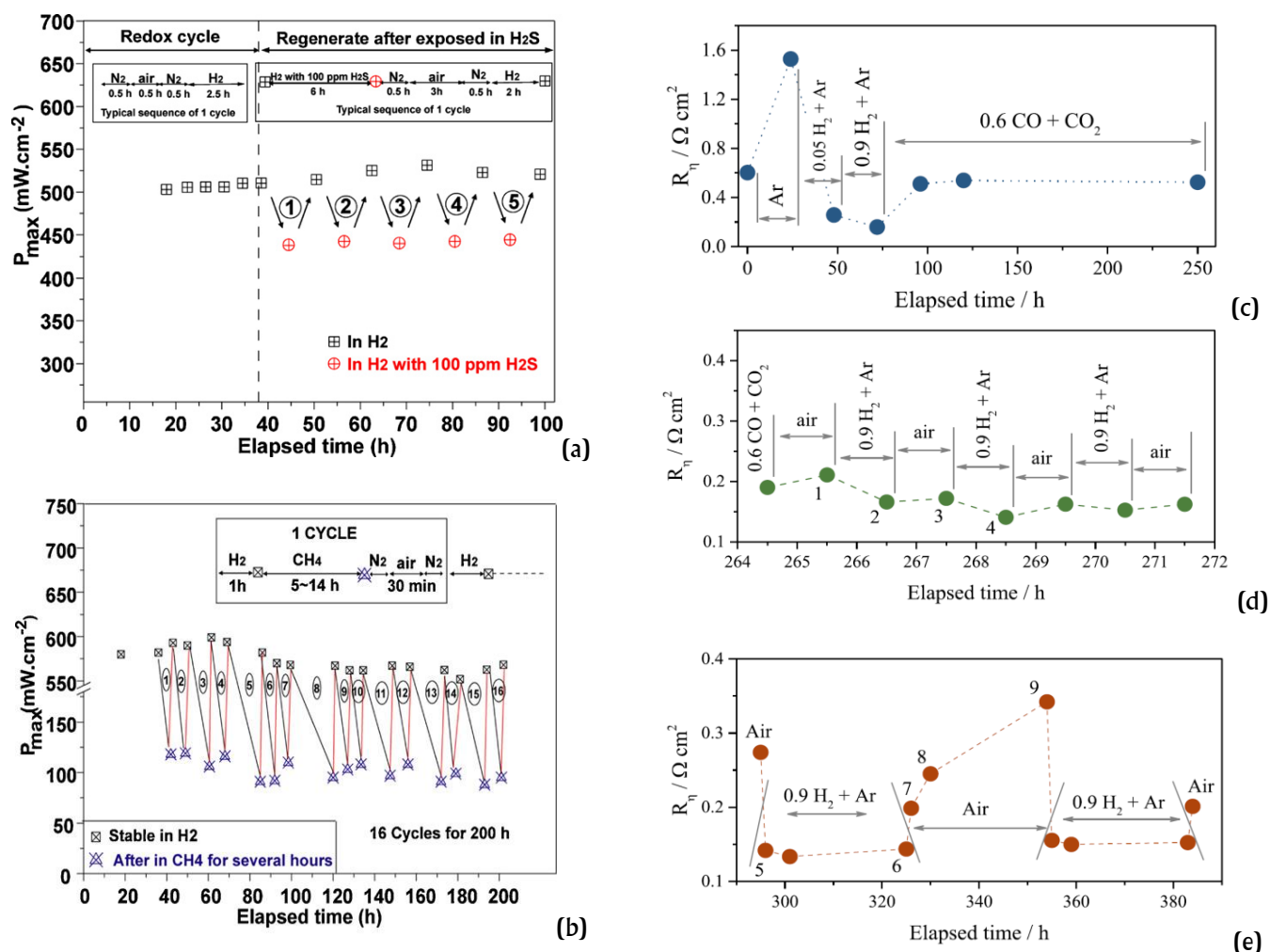


Figure 3 a) Stability of the SFM|LSGM|SFM symmetric cell with $Sr_2Fe_{1.5}Mo_{0.5}O_{6-\delta}$ anode at $800^\circ C$ versus the time of stream after 10 cycles in H_2/CH_4 and b) after 16 cycles, in H_2 , air and CH_4 [49] Copyright © 2011 Elsevier B.V.; Long-term tests of the polarization resistance of the SFM|LSGM|SFM symmetric cell at $800^\circ C$ in c) $H_2/Ar-CO/CO_2$, d) $CO/CO_2-H_2/Ar-air$, e) $H_2/Ar-air$ [90] Copyright © 2019 Elsevier B.V.

test was started, and the maximum power output of the cell did not change significantly after 16 regeneration cycling tests that lasted for 200 h.

The redox cycling of the $Sr_2Fe_{1.5}Mo_{0.5}O_{6-\delta}$ electrode in contact with the $LaGaO_3$ -based electrolyte was performed at $800^\circ C$ in air- CO/CO_2 - Ar/H_2 [90]. A long-term exposure in $0.6CO+0.4CO_2$ did not have any noticeable effect on the polarization resistance of SFM electrode, Figure 3(c). The fast redox cycling had little effect on the activity of the SFM electrodes, the resistance values were satisfactory; after each exposure in air for 1h, the electrode polarization resistance increased slightly, whereas after an atmosphere of $0.9H_2+Ar$ the polarization resistance decreased, Figure 3(d). In the case of $0.9H_2+Ar$ atmospheres, Figure 3(e), a significant increase in polarization resistance over time was observed after switching the $0.9H_2+Ar$ mixture to an oxidizing atmosphere. The value of polarization resistance decreased significantly within 1h when

switching from air to $0.9H_2+Ar$ and remained almost unchanged during long-term exposure. In [91–93], the analysis of electrochemical impedance spectrum and relaxation time distribution showed that the kinetics of surface/interface oxygen exchange and CO/CO_2 activation process in $Sr_2(Fe,Mo)_2O_{6-\delta}$ oxide can be accelerated by the formation of epitaxially endogenous NiFe alloy nanoparticles on the surface.

In [94], it is shown that the introduction of 500ppm H_2S into the fuel caused degradation of $Sr_2Fe_{1.5}Mo_{0.5}O_{6-\delta}$ anode material in a symmetrical cell with $BaZr_{0.8}Ce_{0.1}Y_{0.1}O_{3-\delta}$ electrolyte during 137h; the anode material degraded by 50% of the maximum power density. The SFM material was reacted with H_2S to form metal sulfides SrS , Fe_3S_4 , Fe_9S_{10} and MoS_2 .

2.3. Modifying the A-sublattice in $Sr_2Fe_{1.5}Mo_{0.5}O_{6-\delta}$

Modification of the divalent strontium sublattice by single- and double-charged cations is well known, and the cations must be close in radius to penetrate the matrix to

form a stable single-phase compound. Alkali metals have a lower valence +1 and a smaller size than the A-sublattice cation, which can increase the number of oxygen vacancies or modify the oxidation degree of the B-sublattice active centers due to charge compensation.

In [95–97], theoretical calculations were carried out to predict the promising use of K-doped $\text{Sr}_2\text{Fe}_{1.5}\text{Mo}_{0.5}\text{O}_{6-\delta}$ as an electrode material for oxygen extraction and reduction reactions (ORR). The catalytic capabilities of Fe/Mo–O₂ terminated (001) surfaces of K-doped $\text{Sr}_2\text{Fe}_{1.5}\text{Mo}_{0.5}\text{O}_{6-\delta}$ were investigated using state-of-the-art density functional theory calculations. The surface reconstruction occurred after the formation of oxygen vacancies along the Mo–O–Fe bonds, where MoO₄ tetrahedra were formed. It was assumed that the highly under-coordinated Fe ions adjacent to such molecules had a very low over-potential for the ORR reaction. In this case, iron ions presented an ideal d-occupancy for ORR catalysis. Cowin P.I. et al. [98] synthesized a series of potassium substituted $\text{Sr}_{1.6}\text{K}_{0.4}\text{Fe}_{1+\gamma}\text{Mo}_{1-\gamma}\text{O}_{6-\delta}$ ($\gamma = 0.2, 0.4, 0.6$) to increase the formability and ionic conductivity of compounds. Synthesis was achieved above 700 °C in 5 % H₂/Ar, albeit with the formation of some impurity phases. Phase stability upon redox cycling was observed for the sample $\text{Sr}_{1.6}\text{K}_{0.4}\text{Fe}_{1.4}\text{Mo}_{0.6}\text{O}_{6-\delta}$. Redox cycling demonstrated a strong dependence on high temperature reduction to achieve high conductivities, with re-reduction at lower temperatures attaining between 0.1 and 58.4 % of the initial conductivity observed after high temperature reduction. The reliance of these compounds on high-temperature reduction is expected to limit their utility as SOFC anode materials, as the vulnerability to oxidation can have disastrous consequences for fuel cell durability.

The substitution of strontium for alkaline-earth elements in the double perovskite oxide has been investigated. In [99–102], $\text{Sr}_{2-x}\text{Ca}_x\text{Fe}_{1.5}\text{Mo}_{0.5}\text{O}_{6-\delta}$ compounds were investigated by characterizing the structural properties, electrical properties, electrochemical characteristics. The limit of formation of single-phase solid solution was determined by no more than $x = 1.0$ per formula unit of the compound. Qiao J. et al. [80] recorded the onset of SrMoO₄ impurity formation starting with calcium doping exceeding $x > 0.8$. The Ca substitution caused a 32.4° [99] and 67.5° [101] peak-shift towards higher angles. This implies that the unit cell shrinks due to the smaller ionic radius of Ca²⁺ (0.99 Å) compared to Sr²⁺ (1.18 Å), and Pnma space group does not change. Xu Z. et al. [100] showed that the

single-phase nature of the materials was preserved at $x \leq 0.75$ under oxidizing conditions, and the SrMoO₄ and Ca₂Fe₂O₅ phases were detected with increasing calcium concentration. Under reducing conditions at temperature above 800 °C starting from the base, the compound formed a small impurity of metallic iron up to $x = 0.5$ and recorded phases SrMoO₄, SrFe₂O₅ and Fe with increasing strontium concentration [100, 102]. The space group was identified as *Pm-3m* in both oxidizing and reducing environments. CaFeO₂ could be formed in a hydrogen atmosphere from $x = 0.2$ [101]. Thermal expansion coefficients (TECs) were found to decrease from $16.33 \times 10^{-6} \text{ K}^{-1}$ to $15.08 \times 10^{-6} \text{ K}^{-1}$ when the Ca-doping increased from 0 to 0.6 [99]. Total conductivity increased as the dopant concentration increased with a maximum value of about 33 S/cm for $\text{Sr}_{1.85}\text{Ca}_{0.15}\text{Fe}_{1.5}\text{Mo}_{0.5}\text{O}_{6-\delta}$ at 800°C in humid (3% H₂O) hydrogen. With further increase in calcium concentration, a slight decrease in conductivity was observed [102]. The authors [99] also reported a nonlinear dependence of $\text{Sr}_{2-x}\text{Ca}_x\text{Fe}_{1.5}\text{Mo}_{0.5}\text{O}_{6-\delta}$ conductivity with increasing calcium content, but only in an oxidizing atmosphere. The maximum conductivity in an oxidizing atmosphere was obtained for a doping level $x=0.4$; the conductivity reached 18.9 S/cm at 550°C, which was considerably higher than that of SFM (11.1 S/cm). These results may be explained by the changes observed in the redox couples proportion by the conductivity being influenced by the electronic conductivity via the $\text{Fe}^{3+} + \text{Mo}^{5+} = \text{Fe}^{2+} + \text{Mo}^{6+}$ process. Fuel cell of the symmetrical $\text{Sr}_{2-x}\text{Ca}_x\text{Fe}_{1.5}\text{Mo}_{0.5}\text{O}_{6-\delta}$ electrode performances were measured both in humidified hydrogen fuels and dry air oxidants at a flow rate [101].

Figure 4(a) summarized the maximum power densities for all symmetrical fuel cells with different Ca²⁺ substitutions at 650–800°C. The samples with $x = 0.6$ exhibited the highest power densities at all temperatures, in agreement with the observed total polarization impedance. In [99], the $\text{Sr}_{1.6}\text{Ca}_{0.4}\text{Fe}_{1.5}\text{Mo}_{0.5}\text{O}_{6-\delta}$ sample showed the lowest interface polarization, the highest conductivity, and a maximum power density of 1.26 W/cm² at 800°C. Figure 4(b) presents the power density and voltage as a function of the current density for NiO–YSZ|YSZ anode-supported cells with a SDC interlayer and a $\text{Sr}_{1.6}\text{Ca}_{0.4}\text{Fe}_{1.5}\text{Mo}_{0.5}\text{O}_{6-\delta}$ cathode.

The solubility threshold of barium is $x = 0.6$, so the formation of SrMoO₄ and BaO impurities is found at $x = 0.8$ [103]. Replacing the A position with Ba leads to a change in the crystal lattice parameters, so that the 32.4°

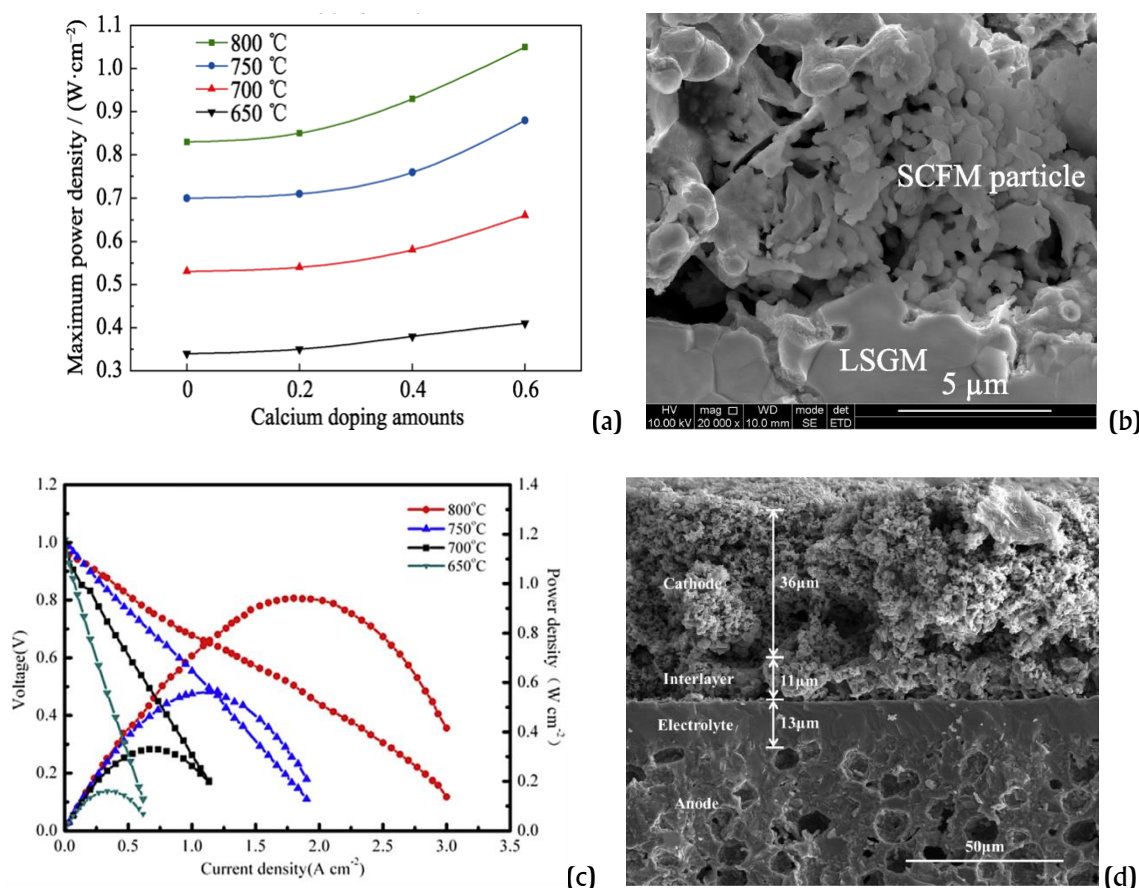


Figure 4 a) Maximum power densities of the symmetrical $\text{Sr}_{2-x}\text{Ca}_x\text{Fe}_{1.5}\text{Mo}_{0.5}\text{O}_{6-\delta}$ electrode cells at different Ca^{2+} substitutions [101], b) Cross-section SEM image of the $\text{LSGM}|\text{Sr}_{2-x}\text{Ca}_x\text{Fe}_{1.5}\text{Mo}_{0.5}\text{O}_{6-\delta}$ interface [101] Copyright © 2019 Editorial Board of Journal of Inorganic Materials; c) I-V and I-P curves of the single cell with $\text{Sr}_{1.6}\text{Ca}_{0.4}\text{Fe}_{1.5}\text{Mo}_{0.5}\text{O}_{6-\delta}$ cathode at 650–800 °C [99], d) Cross-section SEM image of the $\text{NiO-YSZ}|\text{YSZ}|\text{SDC}|\text{Sr}_{1.6}\text{Ca}_{0.4}\text{Fe}_{1.5}\text{Mo}_{0.5}\text{O}_{6-\delta}$ interface [99] Copyright © 2016 Elsevier B.V.

peak is shifted to a smaller angle due to the increase of ionic radius Ba^{2+} (1.35 Å) by Sr^{2+} (1.18 Å). The conductivity of $\text{Sr}_{2-x}\text{Ba}_x\text{Fe}_{1.5}\text{Mo}_{0.5}\text{O}_{6-\delta}$ ceramics reaches its maximum at $\sim 450^\circ\text{C}$, and the conductivity decreases with the increasing temperature due to oxygen evolving out of the lattice with the formation of oxygen vacancies [52]. The conductivity for $x = 0.3\text{--}0.7$ is approximately comparable, the maximum value is 18.5 S/cm at 450°C for $x = 0.7$. For $\text{Sr}_{1.1}\text{Ba}_{0.9}\text{Fe}_{1.5}\text{Mo}_{0.5}\text{O}_{6-\delta}$, the conductivity decreases, and the maximum is 12 S/cm at 400°C . The Ba-doping is observed to significantly reduce the oxygen vacancy formation energy of the host perovskite while increasing the active reaction sites, which leads to a significant decrease in polarization resistance [60]. The anode demonstrates the best catalytic activity when the Ba-doping attains $x = 0.6$. By constructing the $\text{BaCe}_{0.7}\text{Zr}_{0.1}\text{Y}_{0.2}\text{O}_{3-\delta}$ -supported single cells with the configuration $\text{Sr}_{1.4}\text{Ba}_{0.6}\text{Fe}_{1.5}\text{Mo}_{0.5}\text{O}_{6-\delta}|\text{BCZY}|\text{La}_{0.58}\text{Sr}_{0.4}\text{Co}_{0.2}\text{Fe}_{0.8}\text{O}_{3-\delta}+\text{Sm}_{0.2}\text{Ce}_{0.8}\text{O}_{2-\delta}$, the power densities in hydrogen and ethane atmosphere can achieve 205 and 138 mW/cm² at 750°C , respectively, Figure 5. At the

same time, the conversion rate of ethane reaches 38.4% while maintaining the selectivity of ethylene at 95%. Three-electrode half-cell with $\text{Ba}_{0.2}\text{Sr}_{1.8}\text{Fe}_{1.5}\text{Mo}_{0.5}\text{O}_{6-\delta}$ oxide was used to evaluate its electrochemical performance under various steam contents in hydrogen atmosphere both under fuel cell mode and electrolysis mode in [104]. Polarization study showed the monotonously decreased current density in SOFC mode with the increase in the steam content, however, it displayed the opposite trend in the current density in SOEC mode with the suitable steam content at 20%.

When replacing strontium with alkaline-earth elements, it can be concluded that introduction of Ca leads to a reduction of unit cell volume (240.73 \AA^3 to 237.09 \AA^3 from $x = 0$ to 0.6, accordingly); and introduction of Ba has the opposite effect (60.54 \AA^3 to 62.44 \AA^3 from $x = 0$ to 0.6, accordingly), which is connected to the difference in radii of elements in a row Ca–Sr–Ba.

The solubility limit does not exceed $x = 0.8$ regardless of the acceptor impurity. Introduction of

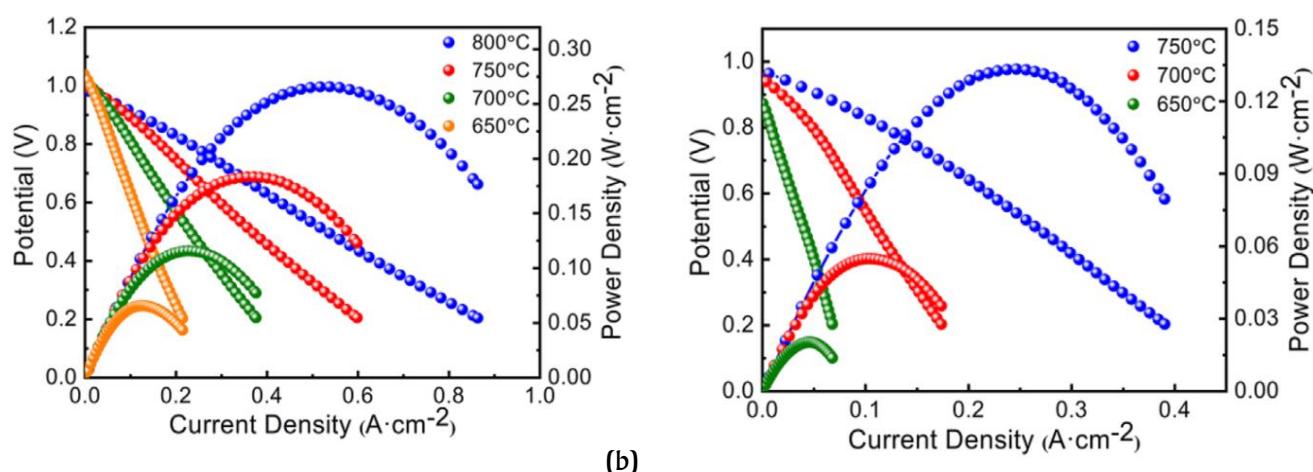


Figure 5 I–V curves and corresponding I–P curves a) in pure hydrogen and b) in dry ethane of the BCZY-supported single cells with the configuration Ba_{0.6}SFM/BCZY/LSCF-SDC [60] Copyright © 2022 The American Ceramic Society.

Table 2 – Total conductivity of A-doped Sr_{2-x}A_xFe_{1.5}Mo_{0.5}O_{6-δ} oxides at 800°C.

Oxide	σ , S/cm	Ref.
Sr _{2-x} Ca _x Fe _{1.5} Mo _{0.5} O _{6-δ} $x = 0.2; 0.4; 0.6$ in air	11; 13; 10.5	99
Sr _{2-x} Ba _x Fe _{1.5} Mo _{0.5} O _{6-δ} $x = 0.3; 0.5; 0.7; 0.9$ in air	11.5; 10.2; 9; 5.5	52
Sr _{2-x} La _x Fe _{1.5} Mo _{0.5} O _{6-δ} $x = 0; 0.05; 0.1$ in CO-CO ₂	12; 11; 8	106
Sr _{2-x} La _x FeCo _{0.5} Mo _{0.5} O _{6-δ} , $x = 0; 0.2; 0.4$ in air	3.62; 3.60; 3.59	62
Sr _{2-x} La _x FeCo _{0.5} Mo _{0.5} O _{6-δ} , $x = 0; 0.2; 0.4$ in H ₂ /Ar	3.57; 3.57; 3.59	62
Sr _{2-x} Sm _x Fe _{1.5} Mo _{0.5} O _{6-δ} , $x = 0; 0.1; 0.2; 0.3; 0.4$ in H ₂	15.9; 22.8; 23.6; 21.7; 21.4	47
Sr _{2-x} Fe _{1.5} Mo _{0.5} O _{6-δ} $x = 0; 0.025; 0.05; 0.075; 0.1$ in air	11; 13; 25; 16; 7.5	111
Sr _{2-x} Fe _{1.4} Ni _{0.1} Mo _{0.5} O _{6-δ} $x = 0.025; 0.05; 0.075; 0.1$ in 5%H ₂ /Ar	25; 26.5; 23.5; 21	113

calcium leads to an increase of total conductivity; maximum is reached at $x = 0.4$, and maximum conductivity for barium is at $x = 0.3$ at temperature 800°C (Table 2).

The A-substitution of Sr₂Fe_{1.5}Mo_{0.5}O_{6-δ} by rare-earth elements such as La, Pr and Sm has been reported in [47, 62, 105–108]. Sun et al. [106] declared single-phase compositions with La at substitution levels of $x = 0.05$ and 0.1 in the Sr_{2-x}La_xFe_{1.5}Mo_{0.5}O_{6-δ} structure. The unit parameter increases from 7.8446 Å for Sr₂Fe_{1.5}Mo_{0.5}O_{6-δ} to 7.8546 Å for Sr_{1.9}La_{0.1}Fe_{1.5}Mo_{0.5}O_{6-δ}, implying that the substitution of Sr with La increases the unit parameter. However, shrinkage of unit volume should be expected in terms of the ionic size effect, because the radius of La³⁺ is slightly smaller than that of Sr²⁺ (1.36 Å and 1.44 Å, respectively). The content of Fe²⁺/Mo⁵⁺ might increase after La³⁺ doping at Sr-substitution, leading to expansion of unit parameters, because the radius of Fe²⁺/Mo⁵⁺ is higher than that of Fe³⁺/Mo⁶⁺. Lanthanum- and nickel-substituted La_xSr_{2-3x/2}Fe_{1.5}Ni_{0.1}Mo_{0.4}O_{6-δ} (La_xSFNM) at $x = 0, 0.1, 0.2, 0.3, 0.4$ are single perovskite structure with cubic symmetry [105]. Both XRD and SEM observations confirm the dissolution of nanosized FeNi₃ particles on the oxide

surface after thermal treatment in H₂. Increasing the La³⁺ content increases the structural stability of these oxides and prevents the dissolution of FeNi₃ nanoparticles. Codoping of lanthanum and cobalt in the structure of double perovskite Sr_{2-x}La_xFeCo_{0.5}Mo_{0.5}O_{6-δ}, $x = 0.0, 0.2,$ and 0.4 results in the formation of stable single-phase solutions in *Fm-3m* space group; the sample with $x = 0.4$ contains a small amount of an impurity phase, which crystallizes in the orthorhombically distorted perovskite-type structure. The single-phase sintering of Sr_{1.5}La_{0.5}Fe_{1.5}Mo_{0.5}O_{6-δ} in air, 5%H₂-95%N₂ and N₂ has been analyzed [109]. In the N₂ environment, the powder is single-phase with *Pm-3m* space group and $a = 3.93584(2)$ Å; in 5%H₂-95%N₂, the synthesized material is far from the perovskite structure. According to the XRD data analysis, the powder after 5%H₂-95%N₂ is composed of pure metal iron Fe, LaSrFeO₄, Sr₃Fe₂O₆ and SrMoO₃. The crystal structure of the powder calcined in air showed more similarity to a cubic perovskite structure, except for several impurity peaks corresponding to SrMoO₄ and LaFeO₃.

Doping with lanthanum [106] slightly reduces the conductivity at 800°C in a 30%CO–CO₂ atmosphere from 12 S/cm for Sr₂Fe_{1.5}Mo_{0.5}O_{6-δ} to 8 S/cm

$\text{Sr}_{1.9}\text{La}_{0.1}\text{Fe}_{1.5}\text{Mo}_{0.5}\text{O}_{6-\delta}$ (Table 2). La-doping $\text{Sr}_2\text{Fe}_{1.5}\text{Mo}_{0.5}\text{O}_{6-\delta}$ significantly increases the surface oxygen exchange rate (k) and the bulk diffusion coefficient (D) in CO–CO₂ mixture. Thus, at 700°C, the k values for $\text{Sr}_{2-x}\text{La}_x\text{Fe}_{1.5}\text{Mo}_{0.5}\text{O}_{6-\delta}$ $x = 0, 0.05$ and 0.1 are $9.71 \cdot 10^{-6}$, $2.03 \cdot 10^{-5}$ and $3.39 \cdot 10^{-5}$ cm/s, respectively; and the D values are $6.66 \cdot 10^{-7}$, $7.87 \cdot 10^{-7}$ and $1.18 \cdot 10^{-5}$ cm²/s, respectively. Perovskite oxides $\text{La}_x\text{Sr}_{2-x}\text{Fe}_{1.5}\text{Ni}_{0.1}\text{Mo}_{0.4}\text{O}_{6-\delta}$ (La_xSFNM , $x = 0.1, 0.2, 0.3$ and 0.4) are prepared and evaluated as symmetrical electrodes in solid oxide electrolysis cells for electrochemical reduction of pure CO₂ in [110]. The polarization resistances are 0.07 S·cm² in air and 0.62 S·cm² in 50% CO-50% CO₂ for $\text{La}_{0.3}\text{SFNM}$ electrode at 800°C. An electrolysis current density of 1.17 A/cm² under 800°C at 1.5 V is achieved for the symmetrical SOECs in pure CO₂.

The temperature dependence of the total conductivity of $\text{Sr}_{2-x}\text{La}_x\text{FeCo}_{0.5}\text{Mo}_{0.5}\text{O}_{6-\delta}$, $x = 0.0; 0.2; 0.4$ ceramic samples in air and in the reducing atmosphere Ar/H₂ (8%) is presented in Table 2 [71]. It is observed that the conductivity in air decreases with increasing La³⁺ content. In a reducing atmosphere the conductivity $x = 0.0$ and 0.2 of the oxides is similar and lower than that observed in air, which is due to the significantly lower concentration of charge carriers (Fe⁴⁺) under these conditions. The highest catalytic activity of $\text{Sr}_{1.7}\text{La}_{0.3}\text{Fe}_{1.5}\text{Mo}_{0.4}\text{Ni}_{0.1}\text{O}_{6-\delta}$ ($\text{La}_{0.3}\text{SFNM}$) toward electro-oxidation of hydrogen fuels could be ascribed to the synergy between the exsolved FeNi₃ alloy nanoparticulates and the supporting La_xSFNM oxides, Figure 6(a) and 6(b) [105]. The cell consisting of thin $\text{La}_{0.9}\text{Sr}_{0.1}\text{Ga}_{0.8}\text{Mg}_{0.2}\text{O}_3$ (LSGM) electrolyte with $\text{La}_{0.3}\text{SFNM}$ anode and $\text{SmBa}_{0.5}\text{Sr}_{0.5}\text{Co}_2\text{O}_{6-\delta}$ (SBSC) + LSGM cathode exhibit the highest power densities, 1.26 , 0.90 and 0.52 W/cm² at 750, 650 and 550°C, respectively.

Modifying $\text{Sr}_2\text{Fe}_{1.5}\text{Mo}_{0.5}\text{O}_{6-\delta}$ structure with samarium leads to a reduction of the unit cell parameters with 7.843 Å for $\text{Sr}_2\text{Fe}_{1.5}\text{Mo}_{0.5}\text{O}_{6-\delta}$ to 7.796 Å for $\text{Sr}_{1.6}\text{Sm}_{0.4}\text{Fe}_{1.5}\text{Mo}_{0.5}\text{O}_{6-\delta}$ [47]; and a 32.2° peak shift on the XRD patterns, Figure 6(c). The sample without Sm displays a pure perovskite structure with no detectable impurity peaks, while for samples doped with different contents of Sm, peaks of impurity SrMoO₄ are observed, and the intensities of impurity peaks become stronger with the increase of Sm content. The conductivity of $\text{Sr}_{2-x}\text{Sm}_x\text{Fe}_{1.5}\text{Mo}_{0.5}\text{O}_{6-\delta}$ ($0 \leq x \leq 0.4$) measured in hydrogen environment passes through a maximum at $x = 0.2$, Table 2, demonstrates the conductivity data at 800°C. The maximum value of 25 S/cm is reached at $x = 0.2$ at 850°C. The XPS data show that the Fe²⁺/Mo⁵⁺

concentration increases for $\text{Sr}_{1.8}\text{Sm}_{0.2}\text{Fe}_{1.5}\text{Mo}_{0.5}\text{O}_{6-\delta}$. EIS analysis proves that Sm-doping into $\text{Sr}_2\text{Fe}_{1.5}\text{Mo}_{0.5}\text{O}_{6-\delta}$ helps improve the catalytic activity. The single cell with $\text{Sr}_{1.8}\text{Sm}_{0.2}\text{Fe}_{1.5}\text{Mo}_{0.5}\text{O}_{6-\delta}$ as the anode demonstrates a performance of 459 , 594 , and 742 mW/cm² at 750, 800, and 850°C, respectively, which is better than that of $\text{Sr}_2\text{Fe}_{1.5}\text{Mo}_{0.5}\text{O}_{6-\delta}$ as the anode, Figure 6(d).

Yang et al. [111] obtained a single-phase series of $\text{Sr}_{2-x}\text{Fe}_{1.5}\text{Mo}_{0.5}\text{O}_{6-\delta}$ solid solutions $x = 0, 0.025, 0.05, 0.075, 0.1$. Creation of deficit in the strontium sublattice led to a positive effect on the total conductivity of the oxides, Table 2. The maximum conductivity was observed for $\text{Sr}_{1.95}\text{Fe}_{1.5}\text{Mo}_{0.5}\text{O}_{6-\delta}$ ($\text{Sr}_{1.95}\text{FM}$) in the temperature range 300–850°C, so the maximum was 33 S/cm at 550°C, which was twice higher than for the deficit-free oxide. More vacancies occurred as Sr-site deficiency increased in the $\text{Sr}_{2-x}\text{Fe}_{1.5}\text{Mo}_{0.5}\text{O}_{6-\delta}$ materials, which enhanced the oxygen ion conductivity at some extent. However, the excess oxygen vacancies would produce the association with B-site cations, which could result in the decrease of conductivity. The maximum power densities of a single cell $\text{Sr}_{1.95}\text{FM}|\text{SDC}|\text{ScSZ}|\text{SDC}|\text{Sr}_{1.95}\text{FM}$ at 800°C increased from 896 to 1083 mW/cm² in H₂, Figure 7(a), and the area specific resistance value with $\text{Sr}_{1.95}\text{Fe}_{1.5}\text{Mo}_{0.5}\text{O}_{6-\delta}$ cathode was 0.17 S/cm² at 800°C. Polarization resistance of $\text{Sr}_2\text{Fe}_{1.5}\text{Mo}_{0.5}\text{O}_{6-\delta}$ electrode was higher than that of $\text{Sr}_{1.95}\text{FM}$ in temperature range 700–900°C, Figure 7(b). However, a higher value of the effective activation energy was observed for the deficient oxide [112], approximately 150 kJ/mol against 111 kJ/mol for the basic composition. This indicates that the creation of a strontium deficit leads either to a change in the mechanism of the oxygen reduction reaction and/or to a redistribution of the contributions of stages of the electrode reaction.

A-site deficient $\text{Sr}_{2-x}\text{Fe}_{1.4}\text{Ni}_{0.1}\text{Mo}_{0.5}\text{O}_{6-\delta}$ ($x = 0-0.1$) perovskites have been synthesized and characterized as anode materials for solid oxide fuel cells [113]. With increasing Sr deficiency, the conductivity in 5% H₂/Ar increases significantly, reaching a peak value of 26.6 S/cm at $x = 0.05$, while further increasing of x reduces the conductivity by affecting the mobility of electronic charge carriers. The $\text{La}_{0.9}\text{Sr}_{0.1}\text{Ga}_{0.8}\text{Mg}_{0.2}\text{O}_3$ electrolyte-supported cell with $\text{La}_{0.6}\text{Sr}_{0.4}\text{Fe}_{0.8}\text{Co}_{0.2}\text{O}_{3-\delta}$ cathode and $\text{Sr}_{1.95}\text{Fe}_{1.4}\text{Ni}_{0.1}\text{Mo}_{0.5}\text{O}_{6-\delta}$ anode demonstrates a maximum power density of 606 mW/cm² at 800°C operating in H₂.

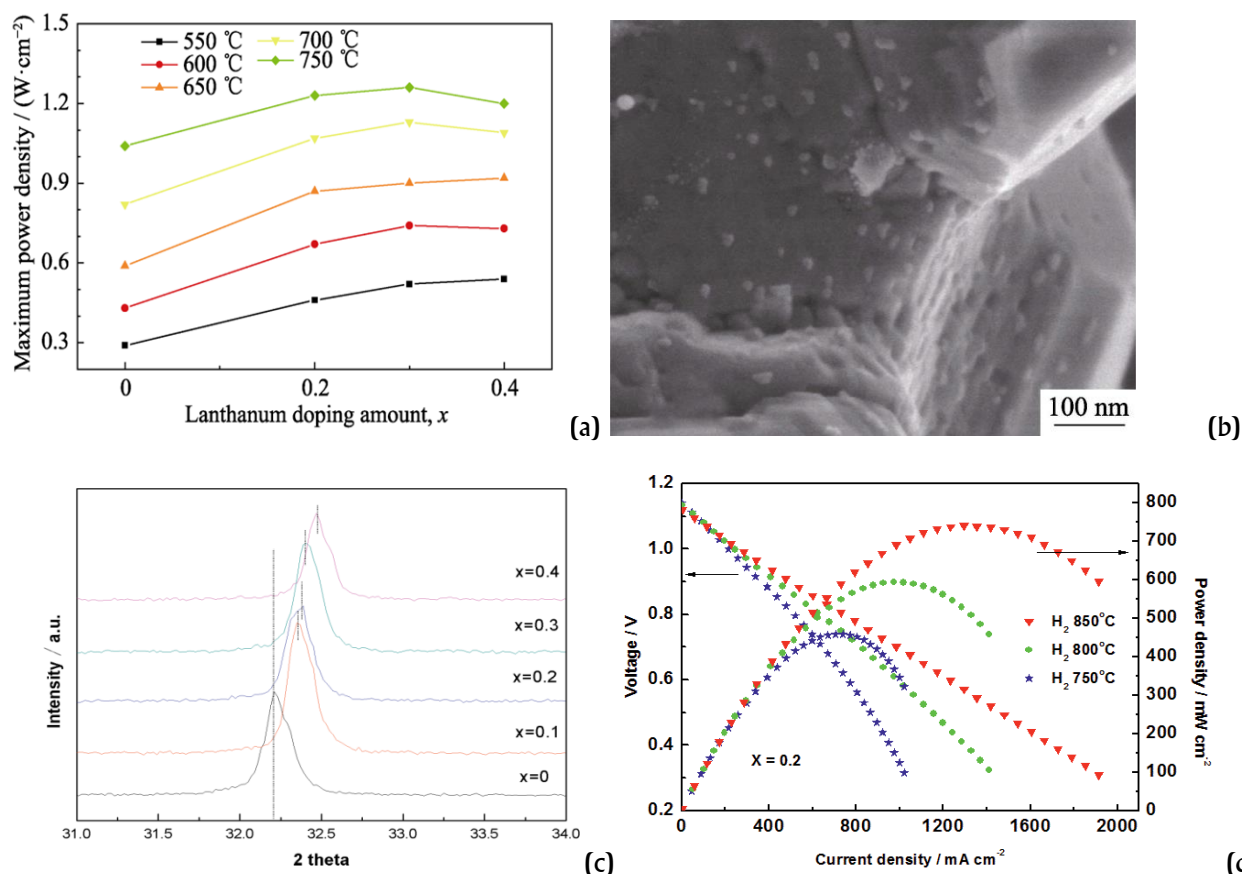


Figure 6 a) Peak power densities at different temperatures for single cells with varied La_xSFNM anodes in 97vol% H_2 -3vol% H_2O [105], b) High magnification view of $\text{Sr}_{1.7}\text{La}_{0.3}\text{FeCo}_{0.5}\text{Mo}_{0.5}\text{O}_{6-\delta}$ anode impregnated Fe-Ni alloy nanoparticles [105] Copyright © 2020 Editorial Board of Journal of Inorganic Materials; c) Angle shift on XRD patterns for $\text{Sr}_{2-x}\text{Sm}_x\text{Fe}_{1.5}\text{Mo}_{0.5}\text{O}_{6-\delta}$ with the increasing Sm content [47], d) $\text{Sr}_{1.8}\text{Sm}_{0.2}\text{Fe}_{1.5}\text{Mo}_{0.5}\text{O}_{6-\delta}$ | LSGM | BSCF cell voltage and power density as functions of current density [47] Copyright © 2014 John Wiley & Sons, Inc.

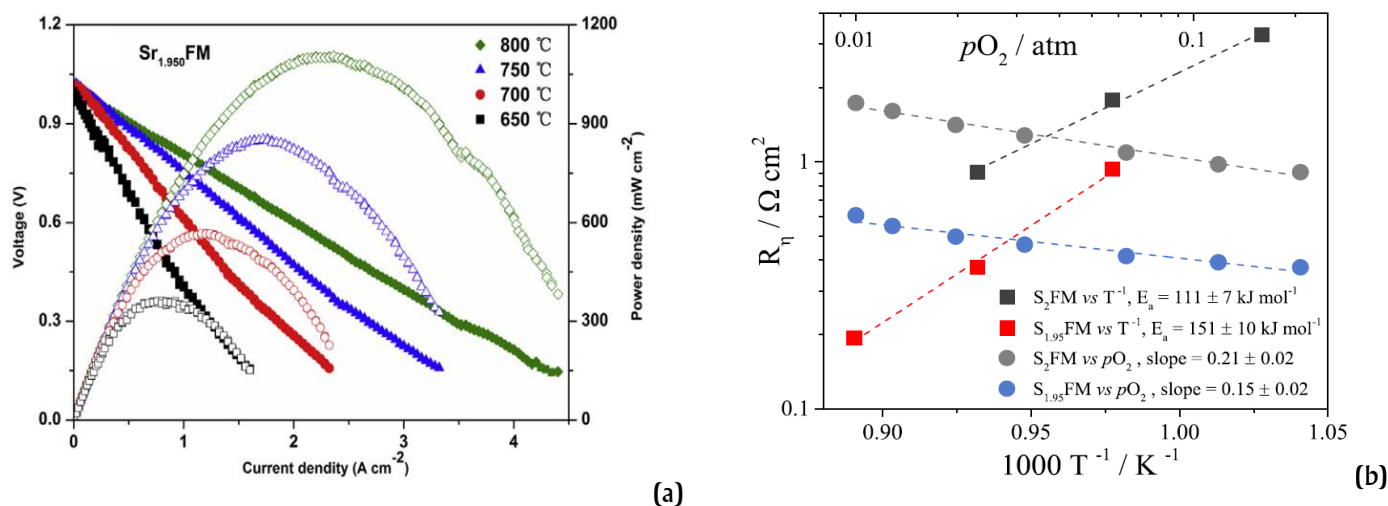


Figure 7 a) I-V and I-P curves of the single cells with $\text{Sr}_{1.95}\text{FM}$ cathode [111] Copyright © 2016 Elsevier B.V.; b) Temperature (squares, at $p_{\text{O}_2} = 0.21$ atm) and concentration (circles, at 800°C) dependencies of the polarization resistance for $\text{Sr}_2\text{Fe}_{1.5}\text{Mo}_{0.5}\text{O}_{6-\delta}$ (S_2FM) and $\text{Sr}_{1.95}\text{Fe}_{1.5}\text{Mo}_{0.5}\text{O}_{6-\delta}$ ($\text{Sr}_{1.95}\text{FM}$) electrodes [112] Copyright © 2022 Elsevier B.V.

2.4. Modifying the B-sublattice in Sr₂Fe_{1.5}Mo_{0.5}O_{6-δ}

The incorporation of cobalt into the iron sublattice is possible in a large concentration range because of the proximity of the ionic radii and the nature of the elements. Pan X. et al. [114] obtained single-phase solutions of Sr₂Fe_{1.5-y}Co_yMo_{0.5}O_{6-δ} at doping $y = 0, 0.5, 1$ by the citrate-nitrate method. However, the introduction of dopant increased the thermal expansion coefficient from $15.8 \cdot 10^{-6}$ to $19.8 \cdot 10^{-6}$ K⁻¹. The total conductivity continuously increased to the maximum value at a temperature range 450–650°C and then decreased when the temperature was increased further. The maximum conductivity was determined for the Sr₂Fe_{0.5}CoMo_{0.5}O_{6-δ} composition of 120 S/cm at 450°C. The trend of a linear threefold increase in conductivity at 800°C is shown in Table 3. The conductivity increase may be due to Co/Fe mixed valence, which was analyzed by XPS method. This means that the small polaron hopping conductivity mechanism exists in Sr₂Fe_{1.5-y}Co_yMo_{0.5}O_{6-δ} materials.

In-situ exsolved CoFe nanoparticles on perovskite matrixes with abundant defects are developed as bifunctional fuel electrocatalysts for reversible solid oxide cells from the Sr₂FeMo_{1-x}Co_xO_{6-δ} [115, 116]. Increase of Co doping promotes CoFe alloy exsolution and the formation of more defects in the remaining perovskite matrix under reducing atmosphere at high temperatures. Consequently, increasing Co dopant content significantly enhance both the electrocatalytic activity towards CO₂ electrolysis and the hydrogen fuel oxidation for the reduced Sr₂FeMo_{1-x}Co_xO_{6-δ}.

Solid solutions with copper Sr₂Fe_{1.5-y}Cu_yMo_{0.5}O_{6-δ} $y = 0, 0.05, 0.1, 0.2, 0.3$ were obtained in [117–119]. The 32.5° diffraction peaks shifted slightly towards a smaller angle as the Cu content increased. This was due to the difference in ionic radius between Cu²⁺ (0.73 Å) and Fe³⁺ (0.645 Å). Therefore, the unit cell of the material expands with increasing amount of Cu doping. The conductivity of Sr₂Fe_{1.5-y}Cu_yMo_{0.5}O_{6-δ} first increases and then decreases with the increasing Cu doping, and it reaches the maximum value of 49.3 S/cm at 450°C for Sr₂Fe_{1.4}Cu_{0.1}Mo_{0.5}O_{6-δ}. The trend of the conductivity as a function of the copper content at 800°C is shown in Table 3. It is evident that the value increases by a factor of five at $y = 0.1$. Hu Ch. et al. [117] showed that the introduction of copper Sr₂Fe_{1.3}Cu_{0.2}Mo_{0.5}O_{6-δ} increased the amount of oxygen vacancies, which significantly improved the chemical adsorption capacity of carbon dioxide at 750°C and its long-term stability, Figure 8. The increased concentration of oxygen vacancies gave additional space for CO₂ adsorption and enhanced the interaction between CO₂ molecules and oxygen vacancies. The higher CO₂ adsorption capacity and desorption temperature improved the high-temperature electrolysis process in SOECs remarkably. The impedance analysis confirmed that the interfacial polarization resistance of the Sr₂Fe_{1.3}Cu_{0.2}Mo_{0.5}O_{6-δ} electrode was significantly lower than that of the SFM electrode, which implies that the intermediate-frequency ion diffusion process has been optimized and has led to improved CO₂ reduction

Table 3 – Total conductivity of B-doped Sr₂Fe_{1.5-y}A_yMo_{0.5}O_{6-δ} oxides at 800°C.

Oxide	σ , S/cm	Ref.
Sr ₂ Fe _{1.5-y} Co _y Mo _{0.5} O _{6-δ} $y = 0; 0.5; 1$ in air	18; 32; 56	114
Sr ₂ Fe _{1.5-y} Cu _y Mo _{0.5} O _{6-δ} $y = 0; 0.05; 0.1; 0.2; 0.3$ in air	5; 7; 25; 23; 10	118
Sr ₂ Fe _{1.5} Mo _{0.5-y} Cu _y O _{6-δ} $y = 0; 0.1; 0.2; 0.3; 0.4; 0.5$ in air	23.4; 34.7; 41.7; 45.7; 71.6; 70.8	119
Sr ₂ Fe _{1.5-y} Ni _y Mo _{0.5} O _{6-δ} $y = 0; 0.05; 0.1; 0.2; 0.4$ in air	11; 16; 32; 31; 20	120
Sr ₂ Fe _{1.5-y} Ni _y Mo _{0.5} O _{6-δ} $y = 0; 0.05; 0.1; 0.2; 0.3$ in H ₂	15.9; 16.4; 20.4; 15.2; 11	121
Sr ₂ Fe _{1.5-y} Nb _y Mo _{0.5} O _{6-δ} $y = 0; 0.1$ in air	10.3; 22.5	57
Sr ₂ Fe _{1.5-y} Nb _y Mo _{0.5} O _{6-δ} $y = 0; 0.1$ in H ₂	16; 25	57
Sr ₂ Fe _{1.5} Mo _{0.5-y} Nb _y O _{6-δ} $y = 0; 0.05, 0.10, 0.15, 0.20$	15; 18; 20; 13.5; 14	130
Sr ₂ Fe _{1.5-y} Sc _y Mo _{0.5} O _{6-δ} $y = 0; 0.05; 0.1$ in air	12; 22; 9	131
Sr ₂ Fe _{1.4} Bi _{0.1} Mo _{0.5} O _{6-δ} in 5% H ₂ / Ar	38	134
Sr ₂ Fe _{1.4} Al _{0.1} Mo _{0.5} O _{6-δ} in 5% H ₂ / Ar	17	134
Sr ₂ Fe _{1.4} Mg _{0.1} Mo _{0.5} O _{6-δ} in 5% H ₂ / Ar	10	134
Sr ₂ Fe _{1-y} TiMo _y O _{6-δ} $y = 0.1; 0.2$ in air	0.92; 0.75	138
Sr ₂ Fe _{1-y} TiMo _y O _{6-δ} $y = 0.1; 0.2$ in H ₂	0.4; 2.2	138
Sr ₂ Fe _{1.5-y} Mn _y Mo _{0.5} O _{6-δ} $y = 0; 0.5$ in 5% H ₂ / Ar	63; 10	141
Sr ₂ Fe _{1.5-y} Mn _y Mo _{0.5} O _{6-δ} $y = 0; 0.5$ in air	10; 3	141

kinetics of the $\text{Sr}_2\text{Fe}_{1.3}\text{Cu}_{0.2}\text{Mo}_{0.5}\text{O}_{6-\delta}$ electrode.

Dissolution of nickel in the iron sublattice $\text{Sr}_2\text{Fe}_{1.5-y}\text{Ni}_y\text{Mo}_{0.5}\text{O}_{6-\delta}$ (SFNM) $y = 0; 0.05; 0.1; 0.2; 0.4$ leads to the formation of a single-phase solid solution in a cubic structure with the space group $Pm\bar{3}m$ after sintering at 950°C in air [120]. Minor amounts of secondary NiO phases are formed when the Ni content reaches 0.5 in air [121]. When the nickel content exceeds $y = 0.2$ in a reducing atmosphere in 3 vol% H_2O humidified hydrogen at 800°C , the secondary phases $\text{Sr}_3\text{FeMoO}_{6.5}$ and Ni are formed. The $\text{Fe}^{3+}/\text{Mo}^{5+}$ ion pair achieves the maximum value at $y = 0.1$, which promotes electron transfer between two ion pairs and improves the reduction/oxidization reaction rate. However, Dai et al. [120] note a linear decrease in the $\text{Fe}^{2+}/\text{Mo}^{6+}$ ion pair in the range of nickel concentrations from 0 to 0.4 in the double perovskite structure. The equilibrium reaction between $\text{Fe}^{3+}/\text{Mo}^{5+}$ and $\text{Fe}^{2+}/\text{Mo}^{6+}$ is disturbed by nickel, which directly affects the conductivity of $\text{Sr}_2\text{Fe}_{1.5-y}\text{Ni}_y\text{Mo}_{0.5}\text{O}_{6-\delta}$ materials. The conductivity of oxides both in air and in hydrogen environment has the same tendency, namely, it increases with introduction of nickel, and maximum conductivity is reached at the introduction of $y = 0.1$ nickel into Fe-sublattice [120, 121].

A further increase in Ni concentration leads to a decrease in conductivity, Table 3, and the conductivity of $\text{Sr}_2\text{Fe}_{1.4}\text{Ni}_{0.1}\text{Mo}_{0.5}\text{O}_{6-\delta}$ (SFN_{0.1}M), which is more than twice the conductivity of $\text{Sr}_2\text{Fe}_{1.5}\text{Mo}_{0.5}\text{O}_{6-\delta}$. Namely, the conductivity of $\text{Sr}_2\text{Fe}_{1.4}\text{Ni}_{0.1}\text{Mo}_{0.5}\text{O}_{6-\delta}$ at 800°C is 32 and 20.4 S/cm in air and hydrogen environment, respectively.

The introduction of nickel $y = 0.1$ and the formation of a strontium deficiency further increases the conductivity of the $\text{Sr}_{1.9}\text{Fe}_{1.4}\text{Ni}_{0.1}\text{Mo}_{0.5}\text{O}_{6-\delta}$ [122]. In an air atmosphere, the maximum conductivity is 30 S/cm at 550°C . Further increases in temperature result in a reduction of the conductivity to 18 S/cm at 800°C . In a hydrogen atmosphere, the conductivity increases linearly in the temperature range $400\text{--}800^\circ\text{C}$, the maximum conductivity is 30 S/cm at 800°C . Since Ni-doping and Sr deficiency can be considered as p -type doping for $\text{Sr}_2\text{Fe}_{1.5}\text{Mo}_{0.5}\text{O}_{6-\delta}$, the improvement in conductivity of $\text{Sr}_{1.9}\text{Fe}_{1.4}\text{Ni}_{0.1}\text{Mo}_{0.5}\text{O}_{6-\delta}$ is observed below 500°C , when the doping is mainly compensated by electron holes; at higher temperatures, ionic charge compensation by oxygen vacancies starts to take effect. $\text{Sr}_{1.95}\text{Fe}_{1.4}\text{Ni}_{0.1}\text{Mo}_{0.5}\text{O}_{6-\delta}$ phase is not stable in the reducing atmosphere [123]. At 800°C , after 10 hours in 5%vol.

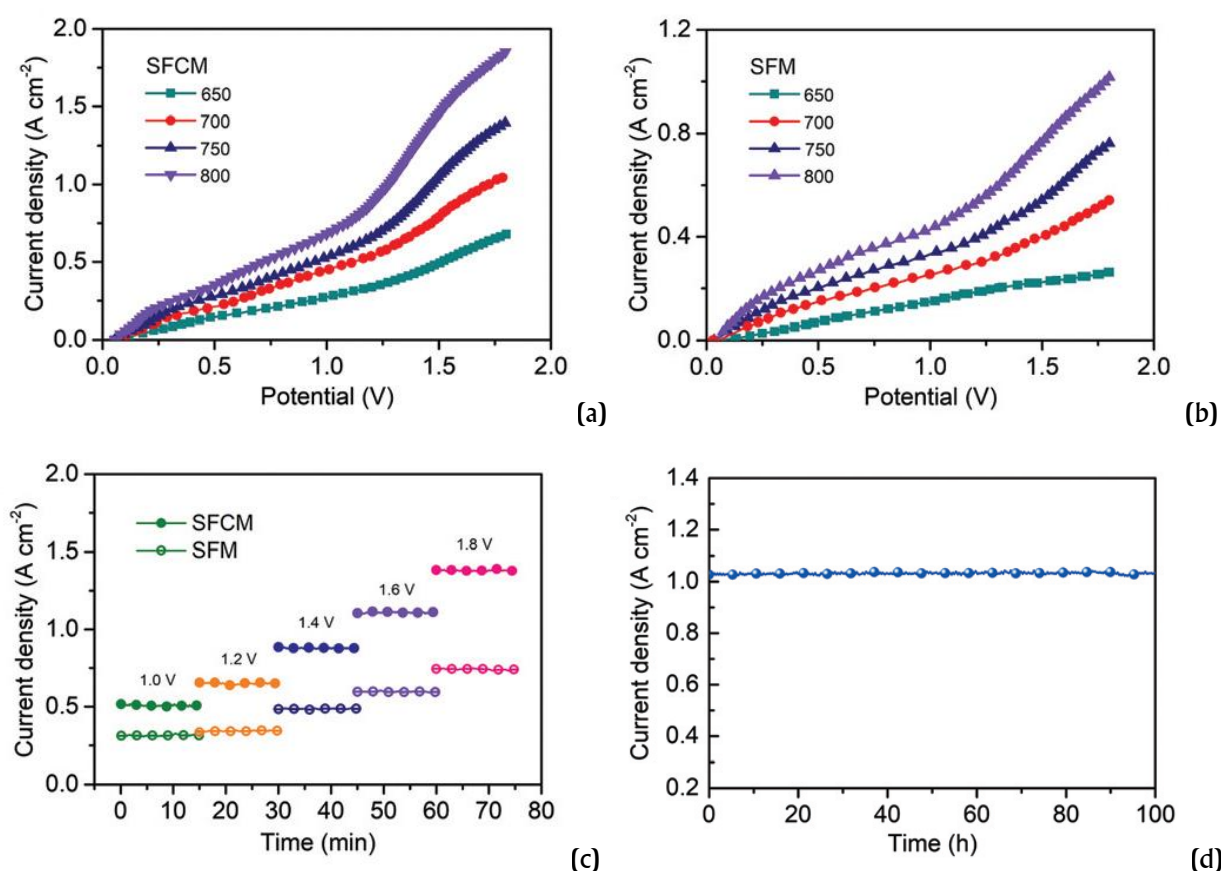


Figure 8 I–V curves of CO₂ electrolysis for (a) $\text{Sr}_2\text{Fe}_{1.3}\text{Cu}_{0.2}\text{Mo}_{0.5}\text{O}_{6-\delta}$ and (b) $\text{Sr}_2\text{Fe}_{1.5}\text{Mo}_{0.5}\text{O}_{6-\delta}$ electrodes; (c) short-term stability 80 h of CO₂ electrolysis at 750°C ; and (d) long-term stability 100 h of CO₂ electrolysis cell with $\text{Sr}_2\text{Fe}_{1.3}\text{Cu}_{0.2}\text{Mo}_{0.5}\text{O}_{6-\delta}$ cathode at 1.5 V, 750°C [117] Copyright © 2019 Royal Society of Chemistry.

a small amount of Fe in the structure. The Fe-Ni alloy and the $\text{Sr}_3\text{FeMoO}_{6.5}$ phase were detected on X-ray in a humid H_2 atmosphere after 10 hours of exposure.

Power density data are available for $\text{Sr}_2\text{Fe}_{1.4}\text{Ni}_{0.1}\text{Mo}_{0.5}\text{O}_{6-6}$ as cathode and anode material [120, 121, 124, 125]. The maximum single cell power density of $\text{SFN}_{0.1}\text{M}|\text{SDC}|\text{YSZ}|\text{NiO}-\text{YSZ}$ is 0.92 and 1.27 W/cm^2 at 700 and 750°C, respectively [120], where $\text{SFN}_{0.1}\text{M}$ is the cathode material, Figure 9(a). The maximum power densities of single cells $\text{SFNM}|\text{LSGM}|\text{SFN}_{0.1}\text{M}$ are demonstrated in Figure 9(b), with SFNM ($\gamma = 0-0.2$) anodes and $\text{Sr}_2\text{Fe}_{1.4}\text{Ni}_{0.1}\text{Mo}_{0.5}\text{O}_{6-6}$ cathode [121].

In [126], a stoichiometric double perovskite $\text{Sr}_2\text{Fe}_{1.5}\text{Mo}_{0.5}\text{O}_{6-6}$ with metal nanoparticles dissolved *in situ* on the surface without reducing phase transition treatment was investigated with the aim of using it as a SOEC cathode for CO_2 reduction reaction (CO_2RR). Nickel was introduced into the B-sublattice during synthesis to obtain a stoichiometric $\text{Sr}_2\text{Fe}_{1.35}\text{Mo}_{0.45}\text{Ni}_{0.2}\text{O}_{6-6}$. The FeNi_3 alloy nanoparticles were exsolved *in situ* and homogeneously fixed on the

perovskite surface via a high-temperature reduction treatment. The interface between the *in situ* dissolved FeNi_3 nanoparticles and the $\text{Sr}_2\text{Fe}_{1.35}\text{Mo}_{0.45}\text{Ni}_{0.2}\text{O}_{6-6}$ substrate with many oxygen vacancies not only chemically accommodated the CO_2 molecules, but also improved the CO_2RR efficiency. Cells with the Ni modified ceramic anodes demonstrated relatively good stability in short-term operations when using CH_4 as the fuel [101, 127, 128]. The YSZ-supported electrolyte with (NiFe+SFM)-SDC fuel electrode and LSM-YSZ oxygen electrode showed a significant increase in performance compared to SFM-SDC and other conventional fuel electrodes for direct CO_2 electrolysis [129]. The improvement of the cell performance in direct CO_2 electrolysis could be attributed to the favourable conditions for the chemical adsorption and surface kinetics of CO_2 on the (NiFe+SFM)-SDC fuel electrode. The Faraday efficiency was close to 100%, indicating a high selectivity of CO_2 reduction to CO, Figure 9(c). SOEC achieved a long-term stability of 500 hours of high current operation due to the excellent sintering and

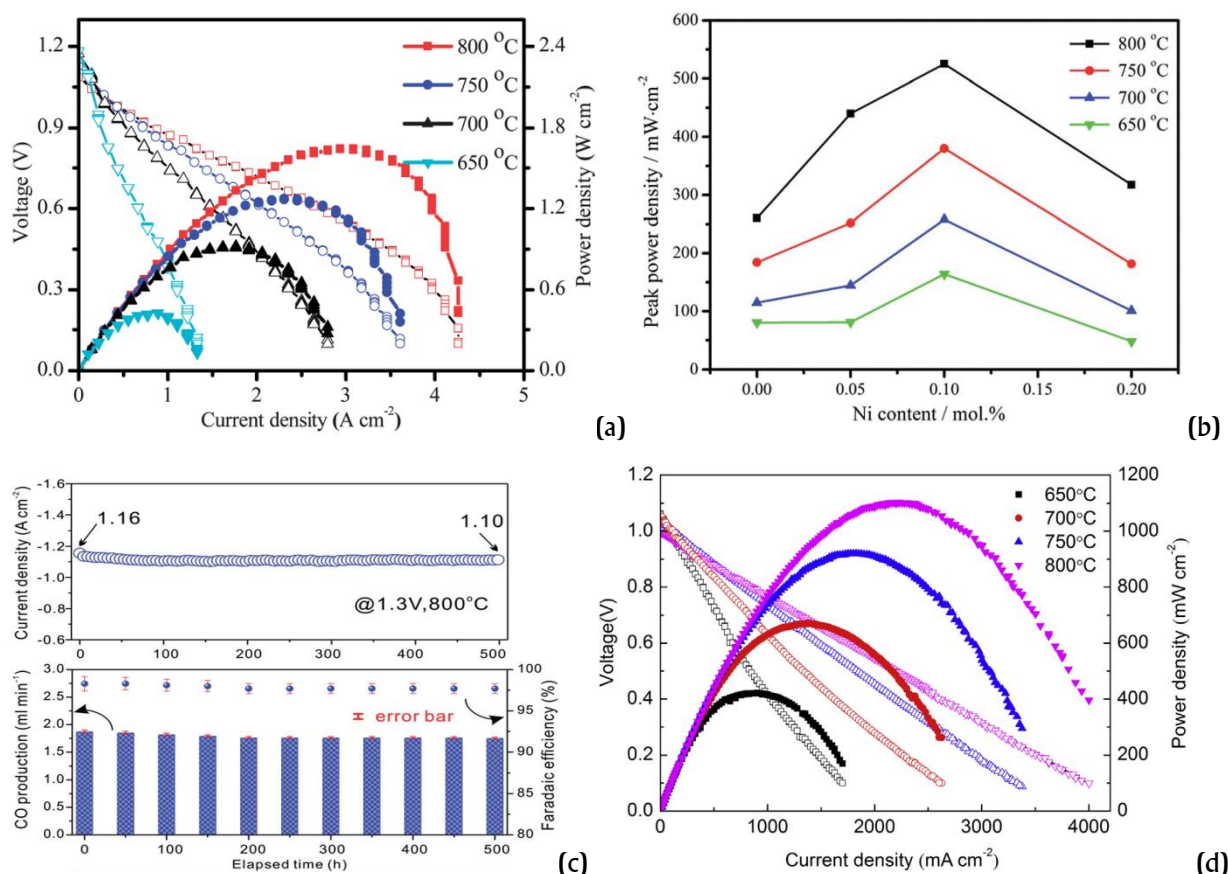


Figure 9 a) I-V and I-P curves of the single cell with the $\text{Sr}_2\text{Fe}_{1.4}\text{Ni}_{0.1}\text{Mo}_{0.5}\text{O}_{6-6}$ cathode at 650–800°C [120] Copyright © 2013 Royal Society of Chemistry; b) Peak power densities of single cells with $\text{SFNM}|\text{LSGM}|\text{Sr}_2\text{Fe}_{1.4}\text{Ni}_{0.1}\text{Mo}_{0.5}\text{O}_{6-6}$ configuration as a function of Ni content in a SFM anode [121] Copyright © 2014 Royal Society of Chemistry; c) Long-term stability test of (NiFe+SFM)-SDC fuel electrode during 500 h for CO_2 electrolysis at 800°C [129] Copyright © 2017 Royal Society of Chemistry; d) I-V and I-P curves of the single cell with the $\text{Sr}_2\text{Fe}_{1.5}\text{Mo}_{0.4}\text{Nb}_{0.1}\text{O}_{6-6}$ cathode at 650–800°C [130] Copyright © 2014 Elsevier B.V.

coking resistance of the (NiFe+SFM) fuel electrode.

Nb-doped double perovskite oxide $\text{Sr}_2\text{Fe}_{1.4}\text{Nb}_{0.1}\text{Mo}_{0.5}\text{O}_{6-\delta}$ had a stable cubic phase with $Fm\bar{3}m$ space group and unit parameter $a = 7.86(2)$ Å in air and $7.87(5)$ Å in hydrogen atmospheres [57]. Good conductivity values were demonstrated in both air (22.5 S/cm) and wet H_2 atmospheres (25 S/cm), Table 3. The maximum power density of a symmetrical cell with $\text{La}_{0.8}\text{Sr}_{0.2}\text{Ga}_{0.83}\text{Mg}_{0.17}\text{O}_3$ electrolyte was estimated to be 531.5 mW/cm^2 at 800°C in H_2 .

More importantly, the symmetrical cell based on $\text{Sr}_2\text{Fe}_{1.4}\text{Nb}_{0.1}\text{Mo}_{0.5}\text{O}_{6-\delta}$ exhibited superior redox stability compared to the $\text{Sr}_2\text{Fe}_{1.5}\text{Mo}_{0.5}\text{O}_{6-\delta}$ material. Among the series of $\text{Sr}_2\text{Fe}_{1.5}\text{Mo}_{0.5-\gamma}\text{Nb}_\gamma\text{O}_{6-\delta}$ ($\gamma = 0.05, 0.10, 0.15, 0.20$) samples [130], $\text{Sr}_2\text{Fe}_{1.5}\text{Mo}_{0.4}\text{Nb}_{0.1}\text{O}_{6-\delta}$ (SFMNb0.10) exhibited the highest conductivity value of 30 S/cm at 550°C , and the lowest area specific resistance of 0.068 S/cm^2 at 800°C . Figure 9(d) shows that the anode-supported single cell with $\text{Sr}_2\text{Fe}_{1.5}\text{Mo}_{0.4}\text{Nb}_{0.1}\text{O}_{6-\delta}$ cathode presented a maximum power density of 1102 mW/cm^2 at 800°C .

$\text{Sr}_2\text{Fe}_{1.5-\gamma}\text{Sc}_\gamma\text{Mo}_{0.5}\text{O}_{6-\delta}$ (SFScM) solid solutions, where $\gamma = 0, 0.05$ and 0.10 , were obtained by a glycine-nitrate combustion method [131, 132]. The formation of scandium oxide impurity phase was found at $\gamma = 0.2$. Scandium doping changed the $\text{Fe}^{2+}/\text{Fe}^{3+}$ and $\text{Mo}^{6+}/\text{Mo}^{5+}$ ratio, which caused a shift in the chemical equilibrium and led to an increase in the electrical conductivity. The electrical conductivity was maximum for $\text{Sr}_2\text{Fe}_{1.45}\text{Sc}_{0.05}\text{Mo}_{0.5}\text{O}_{6-\delta}$ and amounted to 22 S/cm at 800°C in air, which was twice as high as the undoped oxide, Table 3. Analysis of the impedance spectra in [131] shows that the dissociation of adsorbed oxygen at high frequency and the migration of oxygen ions into the TPB at low frequency are the rate limiting stages in the oxygen reduction reaction using SFScM cathodes. The power density obtained in a single cell with SFScM cathode (SFScM|SDC|YSZ|NiO-YSZ) is found to be 1.23 W/cm^2 at 800°C , which significantly exceeds the value of 0.91 W/cm^2 for $\text{Sr}_2\text{Fe}_{1.5}\text{Mo}_{0.5}\text{O}_{6-\delta}$ cathode with the same cell design [131], Figure 10(a). The theoretical calculation results, which are supported by

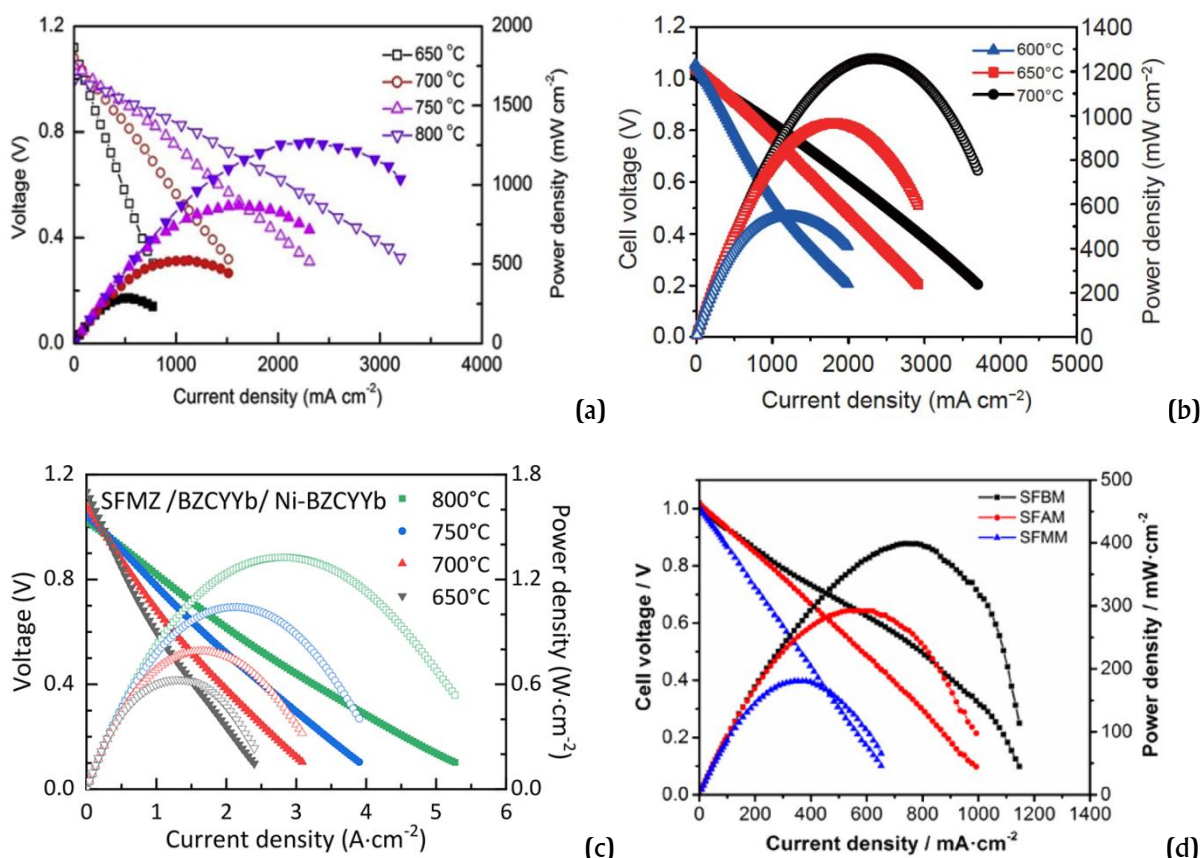


Figure 10 I-V and I-P curves of a) the single cells with the $\text{Sr}_2\text{Fe}_{1.45}\text{Sc}_{0.05}\text{Mo}_{0.5}\text{O}_{6-\delta}$ cathode [131] Copyright © 2017 Elsevier B.V.; b) $\text{Sr}_2\text{Fe}_{1.25}\text{Sc}_{0.05}\text{Mo}_{0.5}\text{O}_{6-\delta}$ cathode [132] Copyright © 2022 Springer Nature Switzerland AG.; c) $\text{Sr}_2\text{Fe}_{1.5}\text{Mo}_{0.4}\text{Zr}_{0.1}\text{O}_{6-\delta}$ cathode [133] Copyright © 2020 American Chemical Society; d) $\text{Sr}_2\text{Fe}_{1.4}\text{Bi}_{0.1}\text{Mo}_{0.5}\text{O}_{6-\delta}$ (SFBM), $\text{Sr}_2\text{Fe}_{1.4}\text{Al}_{0.1}\text{Mo}_{0.5}\text{O}_{6-\delta}$ (SFAM), and $\text{Sr}_2\text{Fe}_{1.4}\text{Mg}_{0.1}\text{Mo}_{0.5}\text{O}_{6-\delta}$ (SFMM) anodes [134] Copyright © 2017 Elsevier B.V.

experimental studies, demonstrate that the $\text{Sr}_2\text{Fe}_{1.25}\text{Sc}_{0.25}\text{Mo}_{0.5}\text{O}_{6-\delta}$ (SFSCo.25M) cathode has a higher proton diffusion rate and a lower polarization resistance than the Sc-free cathode [132]. To evaluate the effectiveness of SFSCo.25M as a cathode for H-SOFCs, $\text{BaCe}_{0.7}\text{Zr}_{0.1}\text{Y}_{0.2}\text{O}_{3-\delta}$ (BCZY) anode-supported half-cells were fabricated using a NiO-BCZY composite anode and BCZY electrolyte. The high performance of the SFSCo.25M cell was demonstrated, Figure 10(b), with maximum power densities of 545, 966 and 1258 mW/cm^2 at 600, 650 and 700°C, respectively.

Zr^{4+} doped $\text{Sr}_2\text{Fe}_{1.5}\text{Mo}_{0.5}\text{O}_{6-\delta}$ is considered as a promising cathode material for proton conducting fuel cells, as it can absorb H_2O . It has been reported [133] that co-regulation of the concentration and basicity of oxygen vacancies can lead to fast proton transport. $\text{Sr}_2\text{Fe}_{1.5}\text{Mo}_{0.4}\text{Zr}_{0.1}\text{O}_{6-\delta}$ (SFMZ) has a large concentration of oxygen vacancies and a strong hydration capacity, which can stimulate the formation of proton defects. SFMZ exhibits improved proton diffusion kinetics, with a value of $8.71 \times 10^{-7} \text{ cm}^2/\text{s}$ at 700°C, comparable to that of the widely used proton electrolyte $\text{BaZr}_{0.1}\text{Ce}_{0.7}\text{Y}_{0.1}\text{Yb}_{0.1}\text{O}_3$ $1.84 \times 10^{-6} \text{ cm}^2/\text{s}$. A low polarization resistance of 0.169 S/cm^2 and a peak power density, Figure 10(c), of 1.35 W/cm^2 were achieved at 800°C with the $\text{Sr}_2\text{Fe}_{1.5}\text{Mo}_{0.4}\text{Zr}_{0.1}\text{O}_{6-\delta}$ cathode.

$\text{Sr}_2\text{Fe}_{1.4}\text{X}_{0.1}\text{Mo}_{0.5}\text{O}_{6-\delta}$ (SFXM, X = Bi, Al and Mg) are considered as anode materials for direct carbon hybrid fuel cells [134]. SFXM powders synthesized by the nitrate combustion method in air at 1050°C are single-phase after 5 hours of exposure. After treatment in 5% H_2/Ar at 800°C for 20 h, the pure SFXM perovskite phase is transformed into $\text{Sr}_3\text{FeMoO}_{6.5}$, followed by an emission of metallic Fe. X-doping significantly changes the $\text{Fe}^{3+}/\text{Fe}^{2+}$ and $\text{Mo}^{6+}/\text{Mo}^{5+}$ ratio towards an increase in Fe^{3+} and Mo^{5+} , which favours the intrinsic conductivity of SFXM, Table 3. The conductivity, catalytic activity, and electrochemical characteristics obey the order $\text{Sr}_2\text{Fe}_{1.4}\text{Bi}_{0.1}\text{Mo}_{0.5}\text{O}_{6-\delta} > \text{Sr}_2\text{Fe}_{1.4}\text{Al}_{0.1}\text{Mo}_{0.5}\text{O}_{6-\delta} > \text{Sr}_2\text{Fe}_{1.4}\text{Mg}_{0.1}\text{Mo}_{0.5}\text{O}_{6-\delta}$. Figure 10(d) demonstrates the dynamic curves for current density versus voltage and current density versus power of a SFXM|LSGM| $\text{La}_{0.6}\text{Sr}_{0.4}\text{Fe}_{0.8}\text{Co}_{0.2}\text{O}_{3-\delta}$ cell with SFXM anodes at 800°C. The maximum power densities of the $\text{La}_{0.8}\text{Sr}_{0.2}\text{Ga}_{0.8}\text{Mg}_{0.2}\text{O}_3$ electrolyte supported single cell with $\text{Sr}_2\text{Fe}_{1.4}\text{Bi}_{0.1}\text{Mo}_{0.5}\text{O}_{6-\delta}$ as the anode reach 399, 287 and 141 mW/cm^2 at 800°C, 750°C and 700°C, respectively. According to experimental investigations and density functional theory calculations [135], Bi-doping could effectively increase the physicochemical properties for CO_2RR , including oxygen vacancy

concentration, CO_2 adsorption capacity, conductivities in $\text{CO}-\text{CO}_2$ atmospheres, oxygen bulk diffusion coefficient, as well as surface exchange coefficient. Du et al. [136] showed that during doping, the Mg and Mo cations are located separately in two different positions B (B and B' in $\text{A}_2\text{BB}'\text{O}_6$), whereas Fe occupies both positions B and B', forming a lattice structure with the form of $\text{Sr}_2(\text{Mg}_{1/3}\text{Fe}_{2/3})(\text{Mo}_{2/3}\text{Fe}_{1/3})\text{O}_{6-\delta}$. Doping with the inactive element Mg not only gives the material excellent redox structural stability, but also causes the creation of anti-nodule defects in the crystal lattice, which give the material excellent electrochemical activity.

There are several papers [61, 137–140] on Ti-substituted double perovskites. $\text{Sr}_2\text{Fe}_{0.75}\text{Ti}_{0.25}\text{MoO}_{6-\delta}$ has a tetragonal symmetry in the $I4/m$ space group with cell parameters $a = 5.3711 \text{ \AA}$, $c = 11.9823 \text{ \AA}$ [61]. The electrical conductivity was found to be $3.78 \times 10^{-5} \text{ S}/\text{cm}$ at 800°C with activation energy of 0.142 eV. Increasing the concentration of titanium leads to a change of the space group from $I4/m$ to $Pm\bar{3}m$. $\text{Sr}_2\text{FeTi}_{0.75}\text{Mo}_{0.25}\text{O}_{6-\delta}$ has a cubic perovskite structure with space group $Pm\bar{3}m$ and cell parameters $a = 3.913(1) \text{ \AA}$, $V = 59.923(0) \text{ \AA}^3$ [139]. The electrical conductivity $\text{Sr}_2\text{FeTi}_{0.75}\text{Mo}_{0.25}\text{O}_{6-\delta}$ passes through a maximum of 2.31 S/cm at 500°C. The polarization resistance of a $\text{Sr}_2\text{FeTi}_{0.75}\text{Mo}_{0.25}\text{O}_{6-\delta}$ cathode on a SDC electrolyte reaches a value of 0.14 $\text{V}\cdot\text{cm}^2$ at 800°C, and peak power density of the electrolyte supported cell with the configuration as NiO-SDC|SDC|SFTM reaches 394 mW/cm^2 at 800°C.

$\text{Sr}_2\text{FeMn}_{0.5}\text{Mo}_{0.5}\text{O}_{6-\delta}$ material possesses cubic lattice [141], B-site cation-disordered $Pm\bar{3}m$ structure with unit cell parameters $a = 3.9127(1) \text{ \AA}$ in air up to high temperatures, and transforms to a B-site cation-ordered structure after reduction in 5 vol% H_2/Ar at 1100°C. The conductivity dependence on the oxygen partial pressure $p\text{O}_2$ shows that oxide has p-type conductivity in air and n-type conductivity under reducing conditions. The Mn-modified oxide shows lower conductivity values than the unmodified compound, thus the conductivity in air and in a hydrogen environment decreases at 800°C, Table 3. In [142], the effectiveness of perovskite-structured $\text{Sr}_2\text{Fe}_{1.4}\text{Mn}_{0.1}\text{Mo}_{0.5}\text{O}_{6-\delta}$ for use as cathode material for CO_2 electrolysis has been investigated. The faster CO_2 reduction kinetics, which is observed for $\text{Sr}_2\text{Fe}_{1.4}\text{Mn}_{0.1}\text{Mo}_{0.5}\text{O}_{6-\delta}$ relative to SFM, is reflected in a lower polarization resistance when both materials are used as single-phase electrodes in symmetrical cells. The polarization resistance in 50% CO/CO_2 at 800°C decreases from 1.15 $\text{S}\cdot\text{cm}^2$ for SFM to 0.60 $\text{S}\cdot\text{cm}^2$ for $\text{Sr}_2\text{Fe}_{1.4}\text{Mn}_{0.1}\text{Mo}_{0.5}\text{O}_{6-\delta}$.

SFM-based perovskite materials are also being

studied as cathode materials in solid oxide electrolytic cells for direct electrolysis of CO_2 , rendering splendid chemical stability under CO_2 atmosphere. A new mixed ionic conductor based on a double perovskite $\text{Sr}_2\text{Fe}_{1.3}\text{Ga}_{0.2}\text{Mo}_{0.5}\text{O}_{6-\delta}$ is considered as cathode material tolerant to CO_2 atmosphere due to its excellent CO_2 adsorption resistance [143]. The maximum power density of $\text{Sr}_2\text{Fe}_{1.3}\text{Ga}_{0.2}\text{Mo}_{0.5}\text{O}_{6-\delta}$ cathode with anode-supported flat-tube (NiO–YSZ) was analyzed in the temperature range 650–800°C, where the anode and cathode were supplied with humidified H_2 (97% H_2 +3% H_2O) and air, respectively. At 750°C, the maximum power density of $\text{Sr}_2\text{Fe}_{1.3}\text{Ga}_{0.2}\text{Mo}_{0.5}\text{O}_{6-\delta}$ cathodes reached 482.4 mW/cm². In [144, 145], it is demonstrated that the *in situ* grown RuFe alloy nanoparticles on the $\text{Sr}_2\text{Fe}_{1.4}\text{Ru}_{0.1}\text{Mo}_{0.5}\text{O}_{6-\delta}$ surface collectively show high and stable electrochemical activity for CO_2 electrolysis in a solid oxide electrolyzer cell.

Sb-doping in SFM improves the anode performance through decreasing the area specific interfacial polarization resistance from 0.184 to 0.075 S·cm² at 800°C [146]. Sb doping greatly improves fuel cell performance, such as increasing the peak power density from 681 to 920 mW/cm² at 800°C with H_2 as the fuel. Meanwhile, improvement is also achieved with syngas and ethanol fuels, generating peak power densities of 765 and 557 mW/cm², respectively.

2.5. Modifying the O-sublattice in $\text{Sr}_2\text{Fe}_{1.5}\text{Mo}_{0.5}\text{O}_{6-\delta}$

Recent research [147–149] has shown that non-metallic elements can be incorporated into the $\text{Sr}_2\text{Fe}_{1.5}\text{Mo}_{0.5}\text{O}_{6-\delta}$ perovskite lattice to modify the surface properties and electronic/phase structure, which is seen as a promising approach to improve the catalytic activity of perovskite-based catalysts. Gao J. et al. [147] show the synthesis of N-doped $\text{Sr}_2\text{Fe}_{1.5}\text{Mo}_{0.5}\text{O}_{6-\delta}$ (SFMON) by ammonolysis, i.e. heat treatment in a continuous ammonia flow of initial SFM powder. By varying the temperature of the powder treatment, it was possible to achieve a nitrogen saturation of up to 11.61 atom% at 550°C, as confirmed by photoelectron spectroscopy. The introduction of N^{3-} into the perovskite lattice due to charge compensation led to an increase in oxygen vacancies and iron concentration in the $\text{Fe}^{3+}/\text{Fe}^{4+}$ high valence state, which enhanced the catalytic activity, Figure 11(a) and 11(b). The content of adsorbed H_2O and hydroxyl groups/adsorbed oxygen was significantly increased in SFMON samples compared to SFM, indicating an improved hydrophilic nature, which may contribute to the adsorption of H_2O and OH- groups on the catalyst surface.

Zhang Y. et al. [148] synthesized chlorine doped oxide $\text{Sr}_2\text{Fe}_{1.5}\text{Mo}_{0.5}\text{O}_{6-x}\text{Cl}_x$ (SFMCl_x, $x = 0, 0.1, 0.2, 0.3, 0.4$). Cl-doping led to an expansion of the crystal lattice ($a = 7.8267 \text{ \AA}$ for SFM and $a = 7.8549 \text{ \AA}$ for SFMCl_{0.4}), weakened the Coulomb force between metal ions and oxygen ions and increased the oxygen mobility of the lattice, thereby improving the electrochemical performance. SFMCl_{0.2} oxide exhibited the best electrochemical performance with the lowest polarization resistance value. The conductivity of SFM and SFMCl_{0.2} oxides was 24 and 15 S/cm at 800°C, respectively. The conductivity of SFMCl_{0.2} was lower than SFM oxide; the introduction of Cl weakened the Fe–O bonds, resulting in an increase in electron localization and a decrease in conductivity. The peak power density of a single cell fabricated with SFMCl_{0.2} cathode increased from 231.5 mW/cm² to 342.2 mW/cm² at 800°C, Figure 11(c). These results show that Cl-doping in SFM is an effective strategy of modifying the electrochemical properties.

Zhang L. et al. [149] investigated the F-doped $\text{Sr}_2\text{Fe}_{1.5}\text{Mo}_{0.5}\text{O}_{6-x}\text{F}_x$ (SFMF_x, $x = 0, 0.1, 0.2, 0.3, 0.4$). The introduction of $x = 0.2$ fluorine enhanced the symmetry of the crystal structure; consequently, the bulk oxygen diffusion and surface oxygen exchange characteristics of the SFM cathode were improved. Electrochemical impedance spectroscopy confirmed that the polarization resistance of the SFM cathode was significantly reduced by F-doping from 0.246 to 0.107 S/cm², respectively. F-doping weakened the bonding between metal cations and oxygen anions, promoting the diffusion process and surface adsorption of oxygen on the cathode. Consequently, the reaction kinetics at the limiting stages was significantly improved. The open-circuit voltage of both single-cells was found to be 1.09 V at 800°C. The peak power density of SFM- and SFMF_{0.2}-based single-cells was found to be 534 and 418 mW/cm², respectively, Figure 11(d). Hence, F-doping significantly enhanced the electrochemical performance of SFM-based cathodes for IT-SOFCs. F-doping and Ni–Fe exsolution enhance CO_2 adsorption and increase the surface reaction rate constant for CO_2RR from $6.79 \cdot 10^{-5}$ to $18.1 \cdot 10^{-5}$ cm/s, as well as the oxygen chemical bulk diffusion coefficient from $9.42 \cdot 10^{-6}$ to $19.1 \cdot 10^{-6}$ cm²/s at 800°C [150]. Meanwhile, the interfacial polarization resistance decreases by 52%, from 0.64 to 0.31 S·cm². At 800°C and 1.5 V, an extremely high current density of 2.66 A/cm² and a stability test over 140 h are achieved for the direct CO_2 electrolysis in the SOEC. Li Y. et al. [151] also confirm a twofold decrease in polarization resistance when the O-sublattice of $\text{Sr}_2\text{Fe}_{1.5}\text{Mo}_{0.5}\text{O}_{6-\delta}\text{F}_{0.1}$ is doped with fluorine.

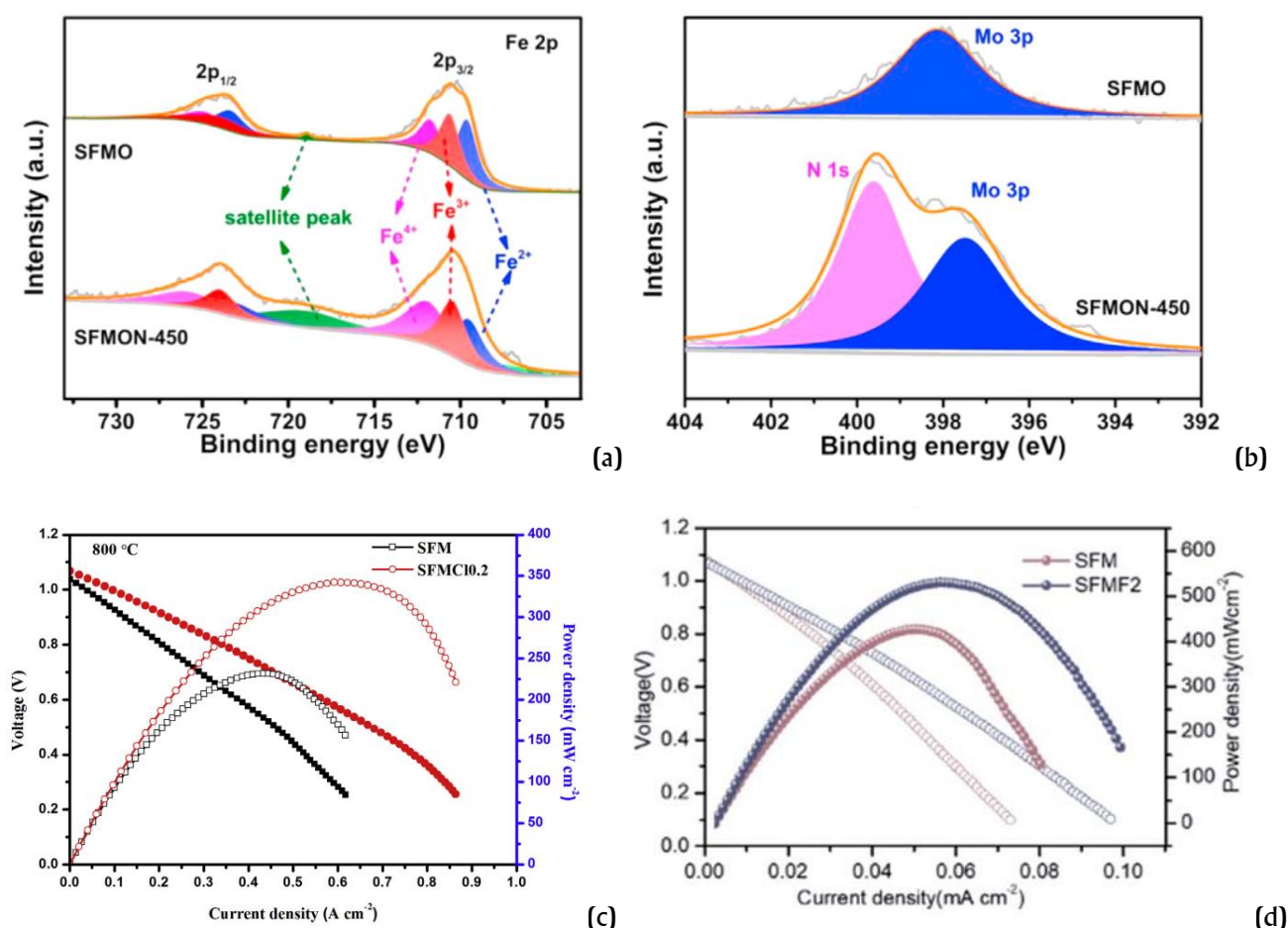


Figure 11 a) High-resolution XPS spectra of Fe $2p$ and b) N $1s$, Mo $3p$ for $\text{Sr}_2\text{Fe}_{1.5}\text{Mo}_{0.5}\text{O}_{6-\delta}$ and N-doped $\text{Sr}_2\text{Fe}_{1.5}\text{Mo}_{0.5}\text{O}_{6-\delta}$ at 450°C [147] Copyright © 2021 Elsevier B.V.; c) I–V and I–P curves of the SFM|LSGM|SFMC $_x$ single cell with the SFMC $_x$ cathode at 800°C [148] Copyright © 2020 Elsevier B.V.; d) the NiO-GDC|GDC|LSGM|GDC|SFMF $_x$ single cell with the SFMF $_x$ cathode at 800°C [149] Copyright © 2020 Royal Society of Chemistry.

3. Conclusions

The review describes transport properties of double perovskite as a promising material for symmetrical solid state electrochemical devices. $\text{Sr}_2\text{Fe}_{1.5}\text{Mo}_{0.5}\text{O}_{6-\delta}$ oxide has a good combination of properties, including electrical conductivity, stability, and catalytic activity in oxidizing and reducing atmospheres. The effect of elemental doping in the A-, B- and O-sublattices on the crystal lattice, conductivity, electrochemical properties, and stability of the materials is considered. Elemental co-doping leads to changes in the valence of iron and molybdenum, thereby increasing catalytic performance and stability and decreasing the thermal expansion coefficient. Today, the knowledge on the nature of the materials based on $\text{Sr}_2\text{Fe}_{1.5}\text{Mo}_{0.5}\text{O}_{6-\delta}$ has been obtained, which confirmed their great potential as promising oxides for the fabrication of symmetric solid oxide cell electrodes. Further development and research in this direction could be useful for the improvement of

electrodes, their stability, and stability in different atmospheres of solid oxide fuel cell operation.

Supplementary materials

No supplementary materials are available.

Funding

This research had no external funding.

Acknowledgments

None.

Author contributions

Natalia Porotnikova: Conceptualization; Writing – original draft.

Denis Osinkin: Supervision; Writing – review & editing.

Conflict of interest

The authors declare no conflict of interest.

Additional information



Natalia Porotnikova;
Ph.D., Lab head;
Laboratory of Cross-Cutting
Technologies in Distributed
Power Generation (InEnergy);
Institute of High Temperature
Electrochemistry Ural Branch
of Russian Academy of
Sciences, Yekaterinburg, Russia.
<https://orcid.org/0000-0001-5284-4553>; Web of Science J-7625-2016



Denis Osinkin;
DSc (Chemistry); Leading
research associate;
Laboratory of Solid State
Oxide Fuel Cells;
Institute of High Temperature
Electrochemistry Ural Branch
of Russian Academy of
Sciences, Yekaterinburg,
Russia.

<https://orcid.org/0000-0001-6396-8551>; Web of Science D-8913-2017

References

- Filippov SP, Yaroslavtsev AB, Hydrogen energy: development prospects and materials, *Russ. Chem. Rev.*, **90**(6) (2021) 627–643. <https://doi.org/10.1070/RCR5014>
- Yakubson KI, Prospects for production and use of hydrogen as one of directions of the development of low-carbon economy in the Russian Federation, *Russ. J. Appl. Chem.*, **93** (2020) 1775–1795. <https://doi.org/10.1134/S1070427220120010>
- Makaryan IA, Sedov IV, Market Potential of Industrial Technologies for Production of Synthetic Bases of Motor Oils, *Russ. J. General Chem.*, **91**(6) (2021) 1243–1259. <https://doi.org/10.1134/S1070363221060414>
- Peng J, Huang J, Wu X, Xu Y, et al., Solid oxide fuel cell (SOFC) performance evaluation, fault diagnosis and health control: A review, *J. Power Sources*, **505** (2021) 230058. <https://doi.org/10.1016/j.jpowsour.2021.230058>
- Simonenko TL, Simonenko NP, Simonenko EP, Sevastyanov VG, et al., Synthesis of Ba_{0.5}Sr_{0.5}Co_{0.8}Fe_{0.2}O_{3-δ} oxide promising as a cathode material of modern solid-oxide fuel cells, *Russ. J. Inorg. Chem.*, **66**(5) (2021) 662–666. <https://doi.org/10.1134/S0036023621050193>
- Gilev AR, Kiselev EA, Cherepanov VA, The Effect of Cobalt Doping on Physicochemical Properties of La_{1.5}Sr_{0.5}Ni_{1-y}Co_yO_{4+d}, *Russ. J. Phys. Chem. A*, **94** (2020) 2474–2481. <https://doi.org/10.1134/S0036024420120110>
- Klyndyuk AI, Zhuravleva YaYu, Gundilovich NN, Crystal structure, thermal and electrotransport properties of NdBa_{1-x}Sr_xFeCo_{0.5}Cu_{0.5}O_{5+δ} (0.02 ≤ x ≤ 0.20) solid solutions *Chim. Tech. Acta*, **8**(3) (2021) 20218301. <https://doi.org/10.15826/chimtech.2021.8.3.01>
- Lyskov NV, Galin MZ, Napolskii PhS, Mazo GN, Increasing the Electrochemical Activity of the Pr_{1.95}La_{0.05}CuO₄ Cathode by Laser Modification of the Electrode/Electrolyte Interface Profile, *Russ. J. Electrochem.*, **58** (2022) 93–99. <https://doi.org/10.1134/S1023193522020070>
- Liu Y, Shao Z, Mori T, Jiang SP, Development of nickel based cermet anode materials in solid oxide fuel cells – Now and future, *Mater. Reports: Energy*, **1**(1) (2021) 100003. <https://doi.org/10.1016/j.matre.2020.11.002>
- Yue W, Li Y, Zheng Y, Wu T, et al., Enhancing coking resistance of Ni/YSZ electrodes: In situ characterization, mechanism research, and surface engineering, *Nano Energy* **62** (2019) 64–78. <https://doi.org/10.1016/j.nanoen.2019.05.006>
- Jiang SP, Sintering behavior of Ni/Y₂O₃-ZrO₂cermet electrodes of solid oxide fuel cells, *J. Mat. Sci.*, **38** (2003) 3775–3782. <https://doi.org/10.1023/A:1025936317472>
- Goodenough JB, Huang YH, Alternative anode materials for solid oxide fuel cells, *J. Power Sources*, **173** (2007) 1–10. <https://doi.org/10.1016/j.jpowsour.2007.08.011>
- Sasaki K, Haga K, Yoshizumi T, Minematsu D, et al., Chemical durability of solid oxide fuel cells: influence of impurities on long-term performance, *J. Power Sources*, **196** (2011) 9130–9140. <https://doi.org/10.1016/j.jpowsour.2010.09.122>
- Skafta TL, Blennow P, Hjelm J, Graves C, Carbon deposition and sulfur poisoning during CO₂ electrolysis in nickel-based solid oxide cell electrodes, *J. Power Sources*, **373** (2018) 54–60. <https://doi.org/10.1016/j.jpowsour.2017.10.097>
- Khrustov AV, Ananyev MV, Bronin DI, Osinkin DA, et al., Characterisation of Ni-cermet degradation phenomena II. Relationship between connectivity and resistivity, *J. Power Sources*, **497** (2021) 229847. <https://doi.org/10.1016/j.jpowsour.2021.229847>
- Osinkin DA, Long-term tests of Ni-Zr_{0.9}Sc_{0.1}O_{1.95} anode impregnated with CeO₂ in H₂+H₂O gas mixtures, *Int. J. Hydrogen Energy*, **41** (2016) 17577–17584. <http://doi.org/10.1016/j.ijhydene.2016.07.136>
- Istomin SYa, Lyskov NV, Mazo GN, Antipov EV, Electrode materials based on complex d-metal oxides for symmetrical solid oxide fuel cells, *Russ. Chem. Rev.*, **90**(6) (2021) 644–676. <https://doi.org/10.1070/RCR4979>
- Zamudio-García J, Caizan-Juanarena L, Porrás-Vázquez JM, Losilla ER, et al., A review on recent advances and trends in symmetrical electrodes for solid oxide cells, *J. Power Sources*, **520** (2022) 230852. <https://doi.org/10.1016/j.jpowsour.2021.230852>
- Ebbesen SD, Jensen SH, Hauch A, Mogensen MB, High Temperature Electrolysis in Alkaline Cells, Solid Proton Conducting Cells, and Solid Oxide Cells, *Chem. Rev.*, **114** (2014) 10697–10734. <https://doi.org/10.1021/cr5000865>
- Shu L, Sunarso J, Hashim SS, Mao J, et al., Advanced perovskite anodes for solid oxide fuel cells: A review, *Int. J. Hydrogen Energy*, **44**(59) (2019) 31275–31304. <https://doi.org/10.1016/j.ijhydene.2019.09.220>
- Zhu K, Luo B, Liu Z, Wen X, Recent advances and prospects of symmetrical solid oxide fuel cells, *Ceram. Int.*,

- 48(7) (2022) 8972–8986.
<https://doi.org/10.1016/j.ceramint.2022.01.258>
22. Kuhn M, Hashimoto S, Sato K, Yashiro K, et al., Oxygen nonstoichiometry, thermo-chemical stability and lattice expansion of $\text{La}_{0.6}\text{Sr}_{0.4}\text{FeO}_{3-\delta}$, *Solid State Ionics*, **195** (2011) 7–15. <https://doi.org/10.1016/j.ssi.2011.05.013>
23. Mosleh M, Sogaard M, Hendriksen PV, Kinetics and Mechanisms of Oxygen Surface Exchange on $\text{La}_{0.6}\text{Sr}_{0.4}\text{FeO}_{3-\delta}$ Thin Films, *J. Electrochem. Soc.*, **156** (2009) B441. <https://doi.org/10.1149/1.3062941>
24. Hashimoto S, Fukuda Y, Kuhn M. Sato K, et al., Oxygen nonstoichiometry and thermo-chemical stability of $\text{La}_{0.6}\text{Sr}_{0.4}\text{Co}_{1-y}\text{Fe}_y\text{O}_{3-\delta}$ ($y = 0.2, 0.4, 0.6, 0.8$), *Solid State Ionics*, **181** (2010) 1713–1719. <https://doi.org/10.1016/j.ssi.2010.09.024>
25. Han Z, Wang Y, Yang Y, Li L, High-performance SOFCs with impregnated $\text{Sr}_2\text{Fe}_{1.5}\text{Mo}_{0.5}\text{O}_{6-\delta}$ anodes toward sulfur resistance, *J. Alloys and Compd.*, **703** (2017) 258–263. <https://doi.org/10.1016/j.jallcom.2017.01.341>
26. Liu GY, Rao GH, Feng XM, Yang HF, et al., Atomic ordering and magnetic properties of non-stoichiometric double-perovskite $\text{Sr}_2\text{Fe}_x\text{Mo}_{2-x}\text{O}_6$, *J. Phys.: Condens. Matter*, **15** (2003) 2053–2060. <https://doi.org/10.1088/0953-8984/15/12/322>
27. Bugaris DE, Hodges JP, Huq A, Chance WM, et al., Investigation of the high-temperature redox chemistry of $\text{Sr}_2\text{Fe}_{1.5}\text{Mo}_{0.5}\text{O}_{6-\delta}$ via in situ neutron diffraction, *J. Mater. Chemistry A*, **2** (2014) 4045–4054. <https://doi.org/10.1039/C3TA14913G>
28. Goldschmidt VM, Die Gesetze der Krystallochemie [The laws of crystallochemistry], *Naturwiss.*, **14** (1926) 477–485. <https://doi.org/10.1007/BF01507527>
29. Longo J, Ward R, Magnetic Compounds of Hexavalent Rhenium with the Perovskite-type Structure, *J. Am. Chem. Soc.*, **83**(13) (1961) 2816–2818. <https://doi.org/10.1021/ja01474a007>
30. Galasso FS, Douglas FC, Kasper RJ, Relationship Between Magnetic Curie Points and Cell Sizes of Solid Solutions with the Ordered Perovskite Structure, *J. Chem. Phys.*, **44** (1966) 1672. <https://doi.org/10.1063/1.1726907>
31. Nakagawa T, Magnetic and electrical properties of ordered perovskite $\text{Sr}_2(\text{FeMo})\text{O}_6$ and its related compounds, *J. Phys. Soc. Jpn.*, **24**(4) (1968) 806–811. <https://doi.org/10.1143/JPSJ.24.806>
32. Bartha C, Plapcianu C, Crisan A, Enculescu M, et al., Structural and magnetic properties of $\text{Sr}_2\text{FeMoO}_6$ obtained at low temperatures, *Dig. J. Nanomater. Bios.*, **11**(3) (2016) 773–780
33. Fang TT, Ko TF, Factors Affecting the Preparation of $\text{Sr}_2\text{Fe}_{2-x}\text{MoxO}_6$, *J. Am. Ceram. Soc.*, **86**(9) (2003) 1453–1455. <https://doi.org/10.1111/j.1151-2916.2003.tb03495.x>
34. Alvarado-Flores JJ, Mondragón-Sánchez R, Ávalos-Rodríguez ML, Alcaraz-Vera JV, et al., Synthesis, characterization and kinetic study of the $\text{Sr}_2\text{FeMoO}_{6-\delta}$ double perovskite: New findings on the calcination of one of its precursors, *Int. J. Hydrogen Energ.*, **46**(51) (2021) 26185–26196. <https://doi.org/10.1016/j.ijhydene.2021.01.191>
35. Miao G, Yuan Ch, Chen T, Zhou Yu, et al., $\text{Sr}_2\text{Fe}_{1+x}\text{Mo}_{1-x}\text{O}_{6-\delta}$ as anode material of cathode-supported solid oxide fuel cells, *Int. J. Hydrogen Energ.*, **41**(2) (2016) 1104–1111. <https://doi.org/10.1016/j.ijhydene.2015.12.045>
36. Yang D, Yang T, Sun Q, Chen Yu, et al., The annealing effects on the crystal structure, magnetism and microstructure of the ferromagnetic double perovskite $\text{Sr}_2\text{FeMoO}_6$ synthesized via spark plasma sintering, *J Alloy. Compd.*, **728** (2017) 337–342. <https://doi.org/10.1016/j.jallcom.2017.09.027>
37. Zhai YQ, Qiao J, Qiu MD, Research on Degradation of Dye Acid Red B by $\text{Sr}_2\text{FeMoO}_6$ Synthesized by Microwave Sintering Method, *E-J. Chem.*, **9**(2) (2012) 818–824. <https://doi.org/10.1155/2012/239305>
38. Santosh M, Lacotte M, David A, Boullay Ph, et al., Pulsed laser deposition of $\text{Sr}_2\text{FeMoO}_6$ thin films grown on spark plasma sintered Sr_2MgWO_6 substrates, *J. Phys. D Appl. Phys.*, **50**(23) (2017) 235301. <https://doi.org/10.1088/1361-6463/aa6e3e>
39. Valdés J, Reséndiz D, Cuán A, Nava R, et al., Sol-Gel Synthesis of the Double Perovskite $\text{Sr}_2\text{FeMoO}_6$ by Microwave Technique, *Materials*, **14**(14) (2021) 3876. <https://doi.org/10.3390/ma14143876>
40. Cernea M, Vasiliu F, Plapcianu C, Bartha C, et al., Preparation by sol-gel and solid state reaction methods and properties investigation of double perovskite $\text{Sr}_2\text{FeMoO}_6$, *J. Eur. Ceram. Soc.*, **33**(13–14) (2013) 2483–2490. <https://doi.org/10.1016/j.jeurceramsoc.2013.03.026>
41. Calleja A, Capdevila XG, Segarra M, Frontera C, et al., Cation order enhancement in $\text{Sr}_2\text{FeMoO}_6$ by water-saturated hydrogen reduction, *J. Eur. Ceram. Soc.*, **31** (2011) 121–127. <https://doi.org/10.1016/j.jeurceramsoc.2010.08.002>
42. Retuerto M, Alonso JA, Martínez-Lope MJ, Martínez JL, et al., Record saturation magnetization, Curie temperature, and magnetoresistance in $\text{Sr}_2\text{FeMoO}_6$ double perovskite synthesized by wet-chemistry techniques, *Appl. Phys. Lett.*, **85** (2004) 266. <https://doi.org/10.1063/1.1772857>
43. Raittila J, Salminen T, Suominen T, Schlesier K, et al., Nanocrystalline $\text{Sr}_2\text{FeMoO}_6$ prepared by citrate-gel method, *J. Phys. Chem. Solids*, **67**(8) (2006) 1712–1718. <https://doi.org/10.1016/j.jpcs.2006.03.009>
44. Xi X, Liu J, Luo W, Fan Y, et al., Unraveling the Enhanced Kinetics of $\text{Sr}_2\text{Fe}_{1+x}\text{Mo}_{1-x}\text{O}_{6-\delta}$ Electrocatalysts for High-Performance Solid Oxide Cells, *Adv. Energy Mater.*, **11**(48) (2021) 2102845. <https://doi.org/10.1002/aenm.202102845>
45. Muñoz-García AB, Bugaris DE, Pavone M, Hodges JP, et al., Unveiling Structure–Property Relationships in $\text{Sr}_2\text{Fe}_{1.5}\text{Mo}_{0.5}\text{O}_{6-\delta}$, an Electrode Material for Symmetric Solid Oxide Fuel Cells, *J. Am. Chem. Soc.*, **134** (2012) 6826–6833. <https://doi.org/10.1021/ja300831k>
46. Markov AA, Leonidov IA, Patrakeev MV, Kozhevnikov VL, et al., Structural stability and electrical transport in $\text{SrFe}_{1-x}\text{MoxO}_{3-\delta}$, *Solid State Ionics*, **179**(21–26) (2008) 1050–1053. <https://doi.org/10.1016/j.ssi.2008.01.026>
47. Wang Y, Li P, Li H, Zhao Y, Li Y, Synthesis and enhanced electrochemical performance of Sm-doped $\text{Sr}_2\text{Fe}_{1.5}\text{Mo}_{0.5}\text{O}_6$, *Fuel Cells*, **14** (2014) 973–978. <https://doi.org/10.1002/fuce.201300250>
48. Osinkin DA, Kolchugin AA, Bogdanovich NM, Beresnev SM, Performance and redox stability of a double-layer $\text{Sr}_2\text{Fe}_{1.5}\text{Mo}_{0.5}\text{O}_{6-\delta}$ -based electrode for solid state electrochemical application, *Electrochim. Acta*, **361** (2020) 137058. <https://doi.org/10.1016/j.electacta.2020.137058>

49. Liu Q, Bugaris DE, Xiao GL, Chmara M, et al., Sr₂Fe_{1.5}Mo_{0.5}O_{6-δ} as a regenerative anode for solid oxide fuel cells, *J. Power Sources*, **196**(22) (2011) 9148–9153. <https://doi.org/10.1016/j.jpowsour.2011.06.085>
50. Retuerto M, Li MR, Go YB, Ignatov A, et al., Magnetic and Structural Studies of the Multifunctional Material SrFe_{0.75}Mo_{0.25}O_{3-δ}, *Inorg. Chem.*, **51**(22) (2012) 12273–12280. <https://doi.org/10.1021/ic301550m>
51. Osinkin DA, Lobachevskaya NI, Sunstov AY, The electrochemical behavior of the promising Sr₂Fe_{1.5}Mo_{0.5}O_{6-δ} + Ce_{0.8}Sm_{0.2}O_{1.9-δ} anode for the intermediate temperature solid oxide fuel cells, *J Alloy. Compd.*, **708** (2017) 451–455. <https://doi.org/10.1016/j.jallcom.2017.03.057>
52. Wang P, Qian W, Xu R, Cheng J, Novel cathode material for solid oxide fuel cells based on Ba-doped Sr₂Fe_{1.5}Mo_{0.5}O₆, *Process. Appl. Ceram.*, **16**(1) (2022) 64–68. <https://doi.org/10.2298/PAC2201064W>
53. Li Ch, Zhang Q, Liu W, Tian X, et al., Tailoring the electrolyte and cathode properties for optimizing the performance of symmetrical solid oxide fuel cells fabricated by one-step cosintering method, *J. Asian Ceram. Soc.*, (2022) 1–10. <https://doi.org/10.1080/21870764.2022.2057640>
54. Wright JH, Virkar AV, Liu Q, Chen F, Electrical characterization and water sensitivity of Sr₂Fe_{1.5}Mo_{0.5}O_{6-δ} as a possible solid oxide fuel cell electrode, *J. Power Sources*, **237** (2013) 13–18. <https://doi.org/10.1016/j.jpowsour.2013.02.079>
55. Xiao G, Liu Q, Zhao F, Zhang L, et al., Sr₂Fe_{1.5}Mo_{0.5}O₆ as cathodes for intermediate-temperature solid oxide fuel cells with La_{0.8}Sr_{0.2}Ga_{0.87}Mg_{0.13}O₃ electrolyte, *J. Electrochem. Soc.*, **158** (2011) B455. <https://doi.org/10.1149/1.3556085>
56. Santos-Gómez L, León-Reina L, Porras-Vázquez JM, Losilla ER, et al., Chemical stability and compatibility of double perovskite anode materials for SOFCs, *Solid State Ionics*, **239** (2013) 1–7. <https://doi.org/10.1016/j.ssi.2013.03.005>
57. Gou M, Ren R, Sun W, Xu C, et al., Nb-doped Sr₂Fe_{1.5}Mo_{0.5}O_{6-δ} electrode with enhanced stability and electrochemical performance for symmetrical solid oxide fuel cells, *Ceram. Int.*, **45** (2019) 15696–15704. <https://doi.org/10.1016/j.ceramint.2019.03.130>
58. Wang Y, Li P, Li H, Zhao Y, et al., Synthesis and enhanced electrochemical performance of Sm-doped Sr₂Fe_{1.5}Mo_{0.5}O₆, *Fuel Cells*, **14**(6) (2014) 973–978. <https://doi.org/10.1002/face.201300250>
59. Li H, Zhao Y, Wang Y, Li Y, Sr₂Fe_{2-x}MoxO_{6-δ} perovskite as an anode in a solid oxide fuel cell: Effect of the substitution ratio, *Catal. Today*, **259**(2) (2016) 417–422. <https://doi.org/10.1016/j.cattod.2015.04.025>
60. Fan Y, Xi X, Li J, Wang Q, et al., Barium-doped Sr₂Fe_{2-x}MoxO_{6-δ} perovskite anode materials for protonic ceramic fuel cells for ethane conversion, *J. Am. Ceram. Soc.*, **105**(5) (2022) 3613–3624. <https://doi.org/10.1111/jace.18329>
61. Karim AH, Abdalla AM, Absah HQHH, Kamis AAM, et al., Synthesis and characterization of Sr₂Fe_{0.75}Ti_{0.25}MoO_{6-δ} as anode for solid oxide fuel cell, *ECS J. Solid State Sci. Technol.*, **26**(1) (2018) 100–106
62. Abdullaev MM, Istomin SYa, Sobolev AV, Presnyakov IA, et al., Synthesis and Study of (Sr,La)₂FeCo_{0.5}Mo_{0.5}O_{6-δ} Oxides with Double Perovskite Structure. *Russ. J. Inorg. Chem.*, **64**(6) (2019) 696–704. <https://doi.org/10.1134/S0036023619060032>
63. Qiu P, Sun Sh, Li J, Jia L., A review on the application of Sr₂Fe_{1.5}Mo_{0.5}O₆-based oxides in solid oxide electrochemical cells, *Sep. Purif. Technol.*, **298** (2022) 121581. <https://doi.org/10.1016/j.seppur.2022.121581>
64. Tomioka Y, Okuda T, Okimoto Y, Kumai R, et al., Magnetic and electronic properties of a single crystal of ordered double perovskite Sr₂FeMoO₆, *Phys. Rev.*, **B61** (2000) 422. <https://doi.org/10.1103/PhysRevB.61.422>
65. Muñoz-García AB, Pavone M, Carter EA, Effect of Antisite Defects on the Formation of Oxygen Vacancies in Sr₂FeMoO₆: Implications for Ion and Electron Transport, *Chem. Mater.*, **23**(20) (2011) 4525–4536. <https://doi.org/10.1021/cm201799c>
66. Muñoz-García AB, Pavone M, Ritzmann AM, Carter EA, Oxide ion transport in Sr₂Fe_{1.5}Mo_{0.5}O_{6-δ}, a mixed ion-electron conductor: new insights from first principles modeling, *Phys. Chem. Phys.*, **15** (2013) 6250–6259. <https://doi.org/10.1039/C3CP50995H>
67. Han Z, Dong H, Wu Y, Yang Y, Locating the rate-limiting step of hydrogen conversion on Sr₂Fe_{1.5}Mo_{0.5}O₆ (001) surface: Implications for efficient SOFC anode design, *Appl. Surf. Sci.*, **595** (2022) 153513. <https://doi.org/10.1016/j.apsusc.2022.153513>
68. Qi H, Lee YL, Yang T, Li W, et al., Positive Effects of H₂O on the Hydrogen Oxidation Reaction on Sr₂Fe_{1.5}Mo_{0.5}O_{6-δ}-Based Perovskite Anodes for Solid Oxide Fuel Cells, *ACS Catal.*, **10**(10) (2020) 5567–5578. <https://doi.org/10.1021/acscatal.9b05458>
69. Ammal SCh, Heyden A, Reaction kinetics of the electrochemical oxidation of CO and syngas fuels on a Sr₂Fe_{1.5}Mo_{0.5}O_{6-δ} perovskite anode, *J. Mater. Chem.*, **A3** (2015) 21618–21629. <https://doi.org/10.1039/C5TA05056A>
70. Liu Q, Dong X, Xiao G, Zhao F, et al., A Novel Electrode Material for Symmetrical SOFCs, *Adv. Mater.*, **22**(48) (2010) 5478–5482. <https://doi.org/10.1002/adma.201001044>
71. Markandeya Y, Reddy YS, Bale S, REDDY CV, et al., Characterization and thermal expansion of Sr₂FexMo_{2-x}O₆ double perovskites, *Bull. Mater. Sci.*, **38**(6) (2015) 1603–1608. <https://doi.org/10.1007/s12034-015-0972-2>
72. Suthirakun S. Rational Design of Perovskite Based Anode Materials For Solid Oxide Fuel Cells: A Computational Approach [dissertation]. Columbia (USA): University of South Carolina; 2013. 193 p.
73. Suthirakun S, Ammal SCh, Muñoz-García AB, Xiao G, et al., Theoretical Investigation of H₂ Oxidation on the Sr₂Fe_{1.5}Mo_{0.5}O₆ (001) Perovskite Surface under Anodic Solid Oxide Fuel Cell Conditions, *J. Am. Chem. Soc.*, **136** (2014) 8374–8386. <https://doi.org/10.1021/ja502629j>
74. Tian H, Li W, Ma L, Yang T, et al., Deconvolution of Water-Splitting on the Triple-Conducting Ruddlesden–Popper-Phase Anode for Protonic Ceramic Electrolysis Cells, *ACS Appl. Mater. Interfaces*, **12** (44) (2020) 49574–49585. <https://doi.org/10.1021/acsami.0c12987>
75. Walker E, Ammal SC, Suthirakun S, Chen F, et al., Mechanism of Sulfur Poisoning of Sr₂Fe_{1.5}Mo_{0.5}O_{6-δ} Perovskite Anode under Solid Oxide Fuel Cell Conditions, *J.*

- Phys. Chem. C, **118(41)** (2014) 23545–23552. <https://doi.org/10.1021/jp507593k>
76. Zhi C, Yang W, Improvement of Mo-doping on sulfur-poisoning of Ni catalyst: Activity and selectivity to CO methanation, *Comput. Theor. Chem.*, **1197** (2021) 113140. <https://doi.org/10.1016/j.comptc.2020.113140>
77. Osinkin DA, Lobachevskaya NI, Bogdanovich NM, Effect of the Copper Oxide Sintering Additive on the Electrical and Electrochemical Properties of Anode Materials Based on Sr₂Fel.5Mo0.5O_{6-δ}, *Russ. J. Appl. Chem.*, **90(10)** (2017) 1686–1692. <https://doi.org/10.1134/S1070427217100196>
78. Osinkin DA, Precursor of Pr₂NiO_{4-δ} as a highly effective catalyst for the simultaneous promotion of oxygen reduction and hydrogen oxidation reactions in solid oxide electrochemical devices, *Int. J. Hydrogen Energ.*, **46** (2021) 24546–24554. <https://doi.org/10.1016/j.ijhydene.2021.05.022>
79. Porotnikova NM, Ananyev MV, Osinkin DA, Khodimchuk AV, et al., Increase in the density of Sr₂Fel.5Mo0.5O_{6-δ} membranes through an excess of iron oxide: The effect of iron oxide on transport and kinetic parameters, *Surf.*, **29** (2022) 101784. <https://doi.org/10.1016/j.surfin.2022.101784>
80. Zhang L, Liu Y, Zhang Y, Xiao G, et al., Enhancement in surface exchange coefficient and electrochemical performance of Sr₂Fel.5Mo0.5O_{6-δ} electrodes by Ce_{0.8}Sm_{0.2}O_{1.9} nanoparticles, *Electrochem. Commun.*, **13(7)** (2011) 711–713. <https://doi.org/10.1016/j.elecom.2011.04.017>
81. Lv H, Zhou Y, Zhang X, Song Y, et al., Infiltration of Ce_{0.8}Gd_{0.2}O_{1.9} nanoparticles on Sr₂Fel.5Mo0.5O_{6-δ} cathode for CO₂ electroreduction in solid oxide electrolysis cell, *J. Energy Chem.*, **35** (2019) 71–78. <https://doi.org/10.1016/j.jechem.2018.11.002>
82. Osinkin DA, Hydrogen oxidation kinetics on a redox stable electrode for reversible solid-state electrochemical devices: The critical influence of hydrogen dissociation on the electrode surface, *Electrochim. Acta*, **389** (2021) 138792. <https://doi.org/10.1016/j.electacta.2021.138792>
83. Xiao J, Han D, Yu F, Zhang L, et al., Characterization of symmetrical SrFe_{0.75}Mo_{0.25}O_{3-δ} electrodes in direct carbon solid oxide fuel cells, *J. Alloy. Compd.*, **688** (2016) 939–945. <https://doi.org/10.1016/j.jallcom.2016.07.223>
84. Gao J, Meng X, Luo T, Wu H, et al., Symmetrical solid oxide fuel cells fabricated by phase inversion tape casting with impregnated SrFe_{0.75}Mo_{0.25}O_{3-δ} (SFMO) electrodes, *Int. J. Hydrogen Energ.*, **42** (2017) 18499–18503. <https://doi.org/10.1016/j.ijhydene.2017.03.205>
85. Li Y, Zou Sh, Ju J, Xi Ch, Characteristics of nano-structured SFM infiltrated onto YSZ backbone for symmetrical and reversible solid oxide cells, *Solid State Ion.*, **319** (2018) 98–104. <https://doi.org/10.1016/j.ssi.2018.02.003>
86. Zhu Z, Sun K, Xu D, Gu Y, et al., Enhancing the performance of symmetrical solid oxide fuel cells with Sr₂Fel.5Mo0.5O_{6-δ} electrodes via infiltration of Pr₆O₁₁ bifunctional catalyst, *Electrochim. Acta*, **402** (2022) 139569. <https://doi.org/10.1016/j.electacta.2021.139569>
87. Li C, Zhang Q, Liu W, Tian X, et al., Tailoring the electrolyte and cathode properties for optimizing the performance of symmetrical solid oxide fuel cells fabricated by one-step co-sintering method, *J. Asian Ceram. Soc.*, **10(2)** (2022) 386–395. <https://doi.org/10.1080/21870764.2022.2057640>
88. Wang Y, Liu T, A highly active and stable Sr₂Fel.5Mo0.5O_{6-δ}-Ce_{0.8}Sm_{0.2}O_{1.95} ceramic fuel electrode for efficient hydrogen production via a steam electrolyzer without safe gas, *Int. J. Coal Sci. Technol.*, **9** (2022) 4. <https://doi.org/10.1007/s40789-022-00470-8>
89. Liu Q, Yang Ch, Dong X, Chen F, Perovskite Sr₂Fel.5Mo0.5O_{6-δ} as electrode materials for symmetrical solid oxide electrolysis cells, *Int. J. Hydrogen Energ.*, **35** (2010) 10039–10044. <https://doi.org/10.1016/j.ijhydene.2010.08.016>
90. Osinkin DA, Kinetics of CO oxidation and redox cycling of Sr₂Fel.5Mo0.5O_{6-δ} electrode for symmetrical solid state electrochemical devices, *J. Power Sources*, **418** (2019) 17–23. <https://doi.org/10.1016/j.jpowsour.2019.02.026>
91. Li Y, Li Y, Zhang S, Ren C, et al., Mutual Conversion of CO–CO₂ on a Perovskite Fuel Electrode with Endogenous Alloy Nanoparticles for Reversible Solid Oxide Cells, *ACS Appl. Mater. Interfaces*, **14(7)** (2022) 9138–9150. <https://doi.org/10.1021/acscami.1c23548>
92. Li Y, Chen X, Yang Y, Jiang Y, Mixed-Conductor Sr₂Fel.5Mo0.5O_{6-δ} as Robust Fuel Electrode for Pure CO₂ Reduction in Solid Oxide Electrolysis Cell, *ACS Sustainable Chem. Eng.*, **5(12)** (2017) 11403–11412. <https://doi.org/10.1021/acssuschemeng.7b02511>
93. Zhang T, Zhal Y, Zhang X, Zhang H, Thermal Stability of an in Situ Exsolved Metallic Nanoparticle Structured Perovskite Type Hydrogen Electrode for Solid Oxide Cells, *ACS Sustainable Chem. Eng.*, **7(12)** (2019) 17834–17844. <https://doi.org/10.1021/acssuschemeng.9b04350>
94. Wachowski S, Li Z, Polfus JM, Norby T, Performance and stability in H₂S of SrFe_{0.75}Mo_{0.25}O_{3-δ} as electrode in proton ceramic fuel cells, *J. Eur. Ceram. Soc.*, **38** (2018) 163–171. <https://doi.org/10.1016/j.jeurceramsoc.2017.08.020>
95. Munoz-Garcia AB, Pavone M, K-doped Sr₂Fel.5Mo0.5O_{6-δ} predicted as a bifunctional catalyst for air electrodes in proton conducting solid oxide electrochemical cells, *J. Mater. Chem.*, **A5** (2017) 12735–12739. <https://doi.org/10.1039/C7TA03340K>
96. Munoz-Garcia AB, Pavone M, First-Principles Design of New Electrodes for Proton-Conducting Solid-Oxide Electrochemical Cells: A-Site Doped Sr₂Fel.5Mo0.5O_{6-δ} Perovskite, *Chem. Mater.*, **28(2)** (2016) 490–500. <https://doi.org/10.1021/acs.chemmater.5b03262>
97. Yang Y, Shi N, Xie Y, Li X, et al., K doping as a rational method to enhance the sluggish air-electrode reaction kinetics for proton-conducting solid oxide cells, *Electrochim. Acta*, **389** (2021) 138453. <https://doi.org/10.1016/j.electacta.2021.138453>
98. Cowin PI, Lan R, Petit CTGP, Wang H, Tao S, Conductivity and redox stability of new double perovskite oxide Sr_{1.6}K_{0.4}Fe_{1+x}Mo_{1-x}O_{6-δ} (x=0.2, 0.4, 0.6), *J. Mater. Sci.*, **51** (2016) 4115–4124. <https://doi.org/10.1007/s10853-016-9734-9>
99. Qiao J, Chen W, Wang W, Wang Z, et al., The Ca element effect on the enhancement performance of Sr₂Fel.5Mo0.5O_{6-δ} perovskite as cathode for intermediate-temperature solid oxide fuel cells, *J. Power Sources*, **331** (2016) 400–407. <https://doi.org/10.1016/j.jpowsour.2016.09.082>
100. Xu Z, Hu X, Wan Y, Xue S, et al., Electrochemical performance and anode reaction process for Ca doped

Sr₂Fe_{1.5}Mo_{0.5}O_{6-δ} as electrodes for symmetrical solid oxide fuel cells, *Electrochim. Acta*, **341** (2020) 136067. <https://doi.org/10.1016/j.electacta.2020.136067>

101. Tian X, Xie M, Ting L, Zhong-Liang Z, Synthesis and Evaluation of Ca-doped Sr₂Fe_{1.5}Mo_{0.5}O_{6-δ} as Symmetrical Electrodes for High Performance Solid Oxide Fuel Cells, *J. Inorg. Mater.*, **34(10)** (2019) 1109–1114. <https://doi.org/10.15541/jim20190067>

102. Osinkin DA, Beresnev SM, Khodimchuk AV, Korzun IV, et al., Functional properties and electrochemical performance of Ca-doped Sr_{2-x}CaxFe_{1.5}Mo_{0.5}O_{6-δ} as anode for solid oxide fuel cells, *J. Solid State Electr.*, **23** (2019) 627–634. <https://doi.org/10.1007/s10008-018-04169-2>

103. Dai N, Wang Z, Jiang T, Feng J, et al., A new family of barium-doped Sr₂Fe_{1.5}Mo_{0.5}O_{6-δ} perovskites for application in intermediate temperature solid oxide fuel cells, *J. Power Sources*, **268** (2014) 176–182. <https://doi.org/10.1016/j.jpowsour.2014.05.146>

104. Kamlungua K, Su PC, Moisture-dependent electrochemical characterization of Ba_{0.2}Sr_{1.8}Fe_{1.5}Mo_{0.5}O_{6-δ} as the fuel electrode for solid oxide electrolysis cells (SOECs), *Electrochim. Acta*, **355** (2020) 136670. <https://doi.org/10.1016/j.electacta.2020.136670>

105. Tian X, Xie M, Ting L, Zhong-Liang Z, La³⁺-substituted Sr₂Fe_{1.5}Ni_{0.1}Mo_{0.4}O_{6-δ} as Anodes for Solid Oxide Fuel Cells, *J. Inorg. Mater.*, **35(5)** (2020) 617–622. <https://doi.org/10.15541/jim20190225>

106. Sun C, Bian L, Qi J, Yu W, et al., An Boosting CO₂ directly electrolysis by electron doping in Sr₂Fe_{1.5}Mo_{0.5}O_{6-δ} double perovskite cathode, *J. Power Sources*, **521** (2022) 230984. <https://doi.org/10.1016/j.jpowsour.2022.230984>

107. Ma J, Tao Z, Kou H, Fronzi M, et al., Evaluating the effect of Pr-doping on the performance of strontium-doped lanthanum ferrite cathodes for protonic SOFCs, *Ceram. Int.*, **46(3)** (2020) 4000–4005. <https://doi.org/10.1016/j.ceramint.2019.10.017>

108. Qi H, Thomas T, Li W, Li W, et al., Reduced Thermal Expansion and Enhanced Redox Reversibility of La_{0.5}Sr_{1.5}Fe_{1.5}Mo_{0.5}O_{6-δ} Anode Material for Solid Oxide Fuel Cells, *ACS Appl. Energy Mater.*, **2(6)** (2019) 4244–4254. <https://doi.org/10.1021/acsaem.9b00494>

109. Qi H, Exsolved nanoparticle decorated redox stable ceramic anode material with high performance for Solid Oxide Fuel Cells [dissertation]. Morgantown (USA): Statler College of Engineering and Mineral Resources; 2019. 135 p.

110. Yue W, Changsong C, Shiwei W, Zhongliang Z, Symmetrical La³⁺-doped Sr₂Fe_{1.5}Ni_{0.1}Mo_{0.4}O_{6-δ} Electrode Solid Oxide Fuel Cells for Pure CO₂ Electrolysis, *J. Inorg. Mater.*, **36(12)** (2021) 1323–1329. <https://doi.org/10.15541/jim20210206>

111. Yang G, Feng J, Sun W, Dai N, et al., The characteristic of strontium-site deficient perovskites Sr_xFe_{1.5}Mo_{0.5}O_{6-δ} (x = 1.9–2.0) as intermediate-temperature solid oxide fuel cell cathodes, *J. Power Sources*, **268** (2014) 771–777. <https://doi.org/10.1016/j.jpowsour.2014.06.129>

112. Osinkin DA, Khodimchuk AV, Antonova EP, Bogdanovich NM, Understanding the oxygen reduction kinetics on Sr_{2-x}Fe_{1.5}Mo_{0.5}O_{6-δ}: Influence of strontium deficiency and correlation with the oxygen isotopic exchange data, *Solid State Ion.*, **374** (2022) 115818. <https://doi.org/10.1016/j.ssi.2021.115818>

113. Feng J, Qiao J, Wang W, Wang Z, et al., Development and performance of anode material based on A-site deficient Sr_{2-x}Fe_{1.4}Ni_{0.1}Mo_{0.5}O_{6-δ} perovskites for solid oxide fuel cells, *Electrochim. Acta*, **215** (2016) 592–599. <https://doi.org/10.1016/j.electacta.2016.08.088>

114. Pan X, Wang Z, He B, Wang S, et al., Effect of Co doping on the electrochemical properties of Sr₂Fe_{1.5}Mo_{0.5}O_{6-δ} electrode for solid oxide fuel cell, *Int. J. Hydrogen Energ.*, **38** (2013) 4108–4115. <https://doi.org/10.1016/j.ijhydene.2013.01.121>

115. Xi X, Wang XW, Fan Y, Wang Q, Efficient bifunctional electrocatalysts for solid oxide cells based on the structural evolution of perovskites with abundant defects and exsolved CoFe nanoparticles, *J. Power Sources*, **482** (2021) 228981. <https://doi.org/10.1016/j.jpowsour.2020.228981>

116. Li Y, Singh M, Zhuang Z, Jing Y, et al., Efficient reversible CO/CO₂ conversion in solid oxide cells with a phase-transformed fuel electrode, *Sci. China Mater.*, **64(5)** (2021) 1114–1126. <https://doi.org/10.1007/s40843-020-1531-7>

117. Xu C, Zhen S, Ren R, Chen H, et al., Cu-doped Sr₂Fe_{1.5}Mo_{0.5}O_{6-δ} as a highly active cathode for solid oxide electrolytic cells, *Chem. Commun.*, **55** (2019) 8009–8012. <https://doi.org/10.1039/C9CC03455B>

118. Tian C, Cheng J, Yang J, A highly active cathode material of Cu-doped Sr₂Fe_{1.5}Mo_{0.5}O_{6-δ} for symmetrical solid oxide fuel cells, *J. Mater. Sci-Mater.*, **E1.32** (2021) 1258–1264. <https://doi.org/10.1007/s10854-020-04898-z>

119. Wang SF, Hsu YF, Huang MS, Chang CW, et al., Characteristics of copper-doped SrFe_{0.75}Mo_{0.25}O_{3-δ} ceramic as a cathode material for solid oxide fuel cells, *Solid State Ion.*, **296** (2016) 120–126. <https://doi.org/10.1016/j.ssi.2016.09.004>

120. Dai N, Feng J, Wang Z, Jiang T, et al., Synthesis and characterization of B-site Ni-doped perovskites Sr₂Fe_{1.5}Mo_{0.5}O_{6-δ} (x = 0, 0.05, 0.1, 0.2, 0.4) as cathodes for SOFCs, *J. Mater. Chem.*, **A1** (2013) 14147–14153. <https://doi.org/10.1039/C3TA13607H>

121. Feng J, Yang G, Dai N, Wang Z, et al., Investigation into the effect of Fe-site substitution on the performance of Sr₂Fe_{1.5}Mo_{0.5}O_{6-δ} anodes for SOFCs, *J. Mater. Chem.*, **A2** (2014) 17628–17634. <https://doi.org/10.1039/C4TA03216K>

122. Xiao G, Wang S, Lin Y, Yang Z, et al., Ni-doped Sr₂Fe_{1.5}Mo_{0.5}O_{6-δ} as Anode Materials for Solid Oxide Fuel Cells, *J. Electrochem. Soc.*, **161(3)** (2013) F305–F310. <https://doi.org/10.1149/2.061403ies>

123. Osinkin DA, Antonova EP, Shubin KS, Bogdanovich NM Influence of nickel exsolution on the electrochemical performance and rate-determining stages of hydrogen oxidation on Sr_{1.95}Fe_{1.4}Ni_{0.1}Mo_{0.5}O_{6-δ} promising electrode for solid state electrochemical devices, *Electrochim. Acta*, **369** (2021) 137673. <https://doi.org/10.1016/j.electacta.2020.137673>

124. Xiao G, Chen F, Ni modified ceramic anodes for direct-methane solid oxide fuel cells, *Electrochem. Commun.*, **13** (2011) 57–59. <https://doi.org/10.1016/j.elecom.2010.11.012>

125. Xiao G, Jin C, Liu Q, Heyden A, et al., Ni modified ceramic anodes for solid oxide fuel cells, *J. Power Sources*, **201** (2012) 43–48. <https://doi.org/10.1016/j.jpowsour.2011.10.103>

126. Lv H, Lin L, Zhang X, Gao D, et al., In situ exsolved FeNi₃ nanoparticles on nickel doped Sr₂Fe_{1.5}Mo_{0.5}O_{6-δ} perovskite for efficient electrochemical CO₂ reduction

- reaction, *J. Mater. Chem.*, **A7** (2019) 11967–11975. <https://doi.org/10.1039/C9TA03065D>
127. Wang Y, Xu J, Meng X, Liu T, et al., Ni infiltrated Sr₂Fe_{1.5}Mo_{0.5}O_{6-δ}-Ce_{0.8}Sm_{0.2}O_{1.9} electrode for methane assisted steam electrolysis process, *Electrochem. Commun.*, **79** (2017) 63–67. <https://doi.org/10.1016/j.elecom.2017.04.018>
128. Gong M, Dai H, A mini review of NiFe-based materials as highly active oxygen evolution reaction electrocatalysts, *Nano Res.*, **8** (2015) 23–39. <https://doi.org/10.1007/s12274-014-0591-z>
129. Li Y, Hu B, Xia C, Xu WQ, et al., A novel fuel electrode enabling direct CO₂ electrolysis with excellent and stable cell performance, *J. Mater. Chem.*, **A5** (2017) 20833–20842. <https://doi.org/10.1039/C7TA05750D>
130. Hou M, Sun W, Li P, Feng J, et al., Investigation into the effect of molybdenum-site substitution on the performance of Sr₂Fe_{1.5}Mo_{0.5}O_{6-δ} for intermediate temperature solid oxide fuel cells, *J. Power Sources*, **272** (2014) 759–765. <https://doi.org/10.1016/j.jpowsour.2014.09.043>
131. Sun W, Li P, Xu C, Dong L, et al., Investigation of Sc doped Sr₂Fe_{1.5}Mo_{0.5}O₆ as a cathode material for intermediate temperature solid oxide fuel cells, *J. Power Sources*, **343** (2017) 237–245. <https://doi.org/10.1016/j.jpowsour.2017.01.063>
132. Zhang L, Yin Y, Xu Y, Yu S, et al., Tailoring Sr₂Fe_{1.5}Mo_{0.5}O_{6-δ} with Sc as a new single-phase cathode for proton-conducting solid oxide fuel cells, *Sci. China Mater.*, **65**(6) (2022) 1485–1494. <https://doi.org/10.1007/s40843-021-1935-5>
133. Ren R, Wang Z, Meng X, Wang X, et al., Tailoring the Oxygen Vacancy to Achieve Fast Intrinsic Proton Transport in a Perovskite Cathode for Protonic Ceramic Fuel Cells, *ACS Appl. Energy Mater.*, **3** (2020) 4914–4922. <https://doi.org/10.1021/acsaem.0c00486>
134. Sun K, Liu J, Feng J, Yuan H, et al., Investigation of B-site doped perovskites Sr₂Fe_{1.4}X_{0.1}Mo_{0.5}O_{6-δ} (X = Bi, Al, Mg) as high-performance anodes for hybrid direct carbon fuel cell, *J. Power Sources*, **365** (2017) 109–116. <https://doi.org/10.1016/j.jpowsour.2017.08.083>
135. Wan Y, Yang Y, Lu Y, Peng R, et al., A Strategy to Enhance the Catalytic Activity of Electrode Materials by Doping Bismuth for Symmetrical Solid Oxide Electrolysis Cells, *ACS Appl. Energy Mater.*, **5**(2) (2022) 2339–2348. <https://doi.org/10.1021/acsaem.1c03822>
136. Du Z, Zhao H, Li S, Zhang Y, et al., Exceptionally High Performance Anode Material Based on Lattice Structure Decorated Double Perovskite Sr₂FeMo_{2/3}Mg_{1/3}O_{6-δ} for Solid Oxide Fuel Cells, *Adv. Energy Mater.*, **8**(18) (2018) 1800062. <https://doi.org/10.1002/aenm.201800062>
137. Feng T, Niu B, Liu J, He T, Sr- and Mo-deficiency Sr_{1.95}Ti_{1-x}Mo_xO_{6-δ} double perovskites as anodes for solid-oxide fuel cells using H₂S-containing syngas, *Int. J. Hydrogen Energ.*, **45** (2020) 23444–23454. <https://doi.org/10.1016/j.ijhydene.2020.06.115>
138. Niu B, Jin F, Zhang L, Shen P, et al., Performance of double perovskite symmetrical electrode materials Sr₂TiFe_{1-x}Mo_xO_{6-δ} (x = 0.1, 0.2) for solid oxide fuel cells, *Electrochim. Acta*, **263** (2018) 217–227. <https://doi.org/10.1016/j.electacta.2018.01.062>
139. Zhou Q, Cheng Y, Li W, Yang X, et al., Investigation of cobalt-free perovskite Sr₂FeTi_{0.75}Mo_{0.25}O_{6-δ} as new cathode for solid oxide fuel cells, *Mater. Res. Bull.*, **74** (2016) 129–133. <https://doi.org/10.1016/j.materresbull.2015.09.023>
140. Xu C, Zhang L, Sun W, Ren R, et al., Co-improving the electrocatalytic performance and H₂S tolerance of a Sr₂Fe_{1.5}Mo_{0.5}O_{6-δ} based anode for solid oxide fuel cells, *J. Mater. Chem. A*, (2022) Advance Article. <https://doi.org/10.1039/D2TA03136A>
141. Zheng K, Swierczek K, Polfus JM, Sunding MF, et al., Carbon Deposition and Sulfur Poisoning in SrFe_{0.75}Mo_{0.25}O_{3-δ} and SrFe_{0.5}Mn_{0.25}Mo_{0.25}O_{3-δ} Electrode Materials for Symmetrical SOFCs, *J. Electrochem. Soc.*, **162**(9) (2015) F1078–F1087. <https://doi.org/10.1149/2.0981509jes>
142. Jiang Y, Yang Y, Xia C, Bouwmeester HJM, Sr₂Fe_{1.4}Mn_{0.1}Mo_{0.5}O_{6-δ} perovskite cathode for highly efficient CO₂ electrolysis, *J. Mater. Chem.*, **A7** (2019) 22939–22949. <https://doi.org/10.1039/C9TA07689A>
143. Xu C, Sun K, Yang X, Ma M, et al., Highly active and CO₂-tolerant Sr₂Fe_{1.3}Ga_{0.2}Mo_{0.5}O_{6-δ} cathode for intermediate-temperature solid oxide fuel cells, *J. Power Sources*, **450** (2020) 227722. <https://doi.org/10.1016/j.jpowsour.2020.227722>
144. Lv H, Lin L, Zhang X, Li R, et al., Promoting exsolution of RuFe alloy nanoparticles on Sr₂Fe_{1.4}Ru_{0.1}Mo_{0.5}O_{6-δ} via repeated redox manipulations for CO₂ electrolysis, *Nat. Commun.*, **12** (2021) 5665. <https://doi.org/10.1038/s41467-021-26001-8>
145. Li B, He S, Li J, Yue X, et al., A Ce/Ru Codoped SrFeO_{3-δ} Perovskite for a Coke-Resistant Anode of a Symmetrical Solid Oxide Fuel Cell, *ACS Catal.*, **10**(24) (2020) 14398–14409. <https://doi.org/10.1021/acscatal.0c03554>
146. Zhang S, Zhu K, Hu X, Peng R, et al., Antimony doping to greatly enhance the electrocatalytic performance of Sr₂Fe_{1.5}Mo_{0.5}O_{6-δ} perovskite as a ceramic anode for solid oxide fuel cells, *J. Mater. Chem.*, **A9** (2021) 24336–24347. <https://doi.org/10.1039/D1TA06196H>
147. Gao J, Zhang Y, Wang X, Jia L, et al., Nitrogen-doped Sr₂Fe_{1.5}Mo_{0.5}O_{6-δ} perovskite as an efficient and stable catalyst for hydrogen evolution reaction, *Mater. Today Energy*, **20** (2021) 100695. <https://doi.org/10.1016/j.mtener.2021.100695>
148. Zhang Y, Zhu Z, Gu Y, Chen H, et al., Effect of Cl doping on the electrochemical performance of Sr₂Fe_{1.5}Mo_{0.5}O_{6-δ} cathode material for solid oxide fuel cells, *Ceram. Int.*, **46** (2020) 22787–22796. <https://doi.org/10.1016/j.ceramint.2020.06.046>
149. Zhang L, Sun W, Xu C, Ren R, et al., Attenuating a metal–oxygen bond of a double perovskite oxide via anion doping to enhance its catalytic activity for the oxygen reduction reaction, *J. Mater. Chem.*, **A8** (2020) 14091–14098. <https://doi.org/10.1039/D0TA04820H>
150. Zhang S, Jiang Y, Han H, Li Y, Perovskite Oxyfluoride Ceramic with In Situ Exsolved Ni-Fe Nanoparticles for Direct CO₂ Electrolysis in Solid Oxide Electrolysis Cells, *ACS Appl. Mater. Interfaces*, **14**(25) (2022) 28854–28864. <https://doi.org/10.1021/acsaami.2c05324>
151. Li Y, Li Y, Wan Y, Xie Y, et al., Perovskite Oxyfluoride Electrode Enabling Direct Electrolyzing Carbon Dioxide with Excellent Electrochemical Performances, **9**(3) (2018) 1803156. <https://doi.org/10.1002/aenm.201803156>